Monthly Notices
of the
ROYAL ASTRONOMICAL SOCIETY

MNRAS **492,** 2095–2118 (2020)
Advance Access publication 2019 December 18

doi:10.1093/mnras/stz3530

Temperature profiles of hot gas in early-type galaxies

Dong-Woo Kim [1]★ Liam Traynor,[1,2] Alessandro Paggi,[1,3,4] Ewan O'Sullivan [1] Craig Anderson,[1] Douglas Burke,[1] Raffaele D'Abrusco [1] Giuseppina Fabbiano,[1] Antonella Fruscione,[1] Jennifer Lauer,[1] Michael McCollough,[1] Douglas Morgan,[1] Amy Mossman,[1] Saeqa Vrtilek[1] and Ginevra Trinchieri[5]

[1] *Harvard-Smithsonian Center for Astrophysics, 60 Garden Street, Cambridge, MA 02138, USA*
[2] *University of Southampton, University Road, Southampton SO17 1BJ, UK*
[3] *INAF-Osservatorio Astrofisico di Torino, via Osservatorio 20, I-10025 Pino Torinese, Italy*
[4] *INFN–Istituto Nazionale di Fisica Nucleare, Sezione di Torino, via Pietro Giuria 1, I-10125 Turin, Italy*
[5] *INAF-Osservatorio Astronomico di Brera, Via Brera 28, I-20121 Milan, Italy*

Accepted 2019 December 12. Received 2019 December 11; in original form 2019 November 1

ABSTRACT

Using the data products of the Chandra Galaxy Atlas (Kim et al.), we have investigated the radial profiles of the hot gas temperature in 60 early-type galaxies (ETGs). Considering the characteristic temperature and radius of the peak, dip, and break (when scaled by the gas temperature and virial radius of each galaxy), we propose a *universal* temperature profile of the hot halo in ETGs. In this scheme, the hot gas temperature peaks at $R_{\rm MAX} = 35 \pm 25$ kpc (or $\sim$0.04 $R_{\rm VIR}$) and declines both inward and outward. The temperature dips (or breaks) at $R_{\rm MIN}$ (or $R_{\rm BREAK}$) = 3–5 kpc (or $\sim$0.006 $R_{\rm VIR}$). The mean slope between $R_{\rm MIN}$ ($R_{\rm BREAK}$) and $R_{\rm MAX}$ is 0.3 ± 0.1. Allowing for selection effects and observational limits, we find that the universal temperature profile can describe the temperature profiles of 72 per cent (possibly up to 82 per cent) of our ETG sample. The remaining ETGs (18 per cent) with irregular or monotonically declining profiles do not fit the universal profile and require another explanation. The temperature gradient inside $R_{\rm MIN}$ ($R_{\rm BREAK}$) varies widely, indicating different degrees of additional heating at small radii. Investigating the nature of the hot core (HC with a negative gradient inside $R_{\rm MIN}$), we find that HC is most clearly visible in small galaxies. Searching for potential clues associated with stellar, active galactic nucleus (AGN) feedback, and gravitational heating, we find that HC may be related to recent star formation. But we see no clear evidence that AGN feedback and gravitational heating play any significant role for HC.

Key words: galaxies: elliptical and lenticular, cD – galaxies: ISM – X-rays: galaxies.

1 INTRODUCTION

The hot gaseous haloes of early-type galaxies (ETGs) provide crucial information for the formation and evolution of the host galaxy. Various physical processes affecting the galaxy evolution are also reflected in the thermal structure of the hot interstellar medium (ISM; e.g. see Kim & Fabbiano 2015). They include mergers, the infall of gas, ram-pressure stripping, sloshing (and other tidal interactions), active galactic nucleus (AGN) feedback, and stellar feedback.

Early models for the hot haloes of ETGs suggested cooling flows because the predicated cooling time is shorter than the Hubble time (e.g. Sarazin & White 1987; Fabian 1994). With a rapid radiative cooling in the central region, these models predict the temperature to rapidly decrease and the surface brightness to strongly peak towards the centre. However, observations have shown that the large amount of expected cool gas is not present, and the cooling occurs on a much smaller scale than predicted (e.g. Fabian 2012, and references therein). This implies that there is a source of internal heating that prevents rapid cooling in the centre of the hot halo. The possible heating mechanisms include AGN feedback (e.g. Fabian 2012), stellar feedback (e.g. Ciotti et al. 1991; Tang & Wang 2005), and gravitational heating (e.g. Khosroshahi et al. 2004; Johansson et al. 2009). Different models predict different temperature profiles. The classical cooling flow model predicts that the temperature peaks at a certain radius and declines both inward and outward (e.g. Sarazin & White 1987; Pellegrini 2012). Recent simulations of

★ E-mail: dkim@cfa.harvard.edu

pure cooling flows indicate that the temperature declines towards the centre, roughly following $T \sim r^{0.5}$ (Gaspari, Ruszkowski & Sharma 2012). In contrast, feedback models predict different degrees of temperature increase towards the centre. Recent hydrodynamic simulations of AGN feedback (e.g. Pellegrini et al. 2012a; Ciotti et al. 2017 – they assume AGN winds, but no jet) show that the gas temperature monotonically decreases to the centre from a few effective radii, but the profile becomes somewhat chaotic during the short period of major bursts. Possible heating mechanisms such as SN heating (e.g. Ciotti et al. 1991; Tang & Wang 2005), gravitational heating from the SMBH (Pellegrini et al. 2012b), and gravitational potential energy during infall (Khosroshahi et al. 2004) are also reflected in the profiles. These models provide an alternative to the cooling flow models. However, they still do not capture the full complexity of the temperature profiles for ETGs, and more comprehensive models are needed to be able to explain all the features seen in these temperature profiles. To advance our understanding of the various mechanisms and to help to leverage various model parameters, it is necessary to provide accurate observational constraints on the T profiles.

It has been suggested that galaxy groups and clusters may have a universal temperature profile (when the core is excluded) that is close to self-similar (e.g. De Grandi & Molendi 2002; Vikhlinin et al. 2005; Sanderson et al. 2006; Sun et al. 2009). In this picture, the temperature is rising rapidly with increasing radius out to $r \sim 0.1\ R_{\rm VIR}$ (viral radius), before slowly decreasing to large radii. The temperature of the gas is primarily governed by the gravity of the groups and clusters. In ETGs (and small groups), however, baryonic physics becomes more important, while the gravitational effects (self-similarity) become less dominant than clusters and large groups. The presence of X-ray cavities hollowed out by radio jets, SN-driven galactic winds, filaments, shells, tidal features, and cold fronts (e.g. Boehringer et al. 1993; Churazov et al. 2001; Gastaldello et al. 2008) all impact the temperature profiles of ETGs, which can vary widely from one galaxy to another. For example, some galaxies show a temperature decrease towards the centre and peaks at large radii, while others show a rising temperature towards their centre (e.g. Diehl & Statler 2008; Pellegrini et al. 2012b). See also O'Sullivan et al. (2017), who found that some groups also show the temperature rising towards the centre.

In this paper, we use a sample of 60 nearby ETGs taken from the Chandra Galaxy Atlas (Kim et al. 2019a) with extended X-ray emission that allows us to extract temperature profiles (see Table 1). As described in Kim et al. (2019a), our sample includes several examples of brightest group/cluster galaxies (BCGs). However, we exclude large groups/clusters by limiting $T_{\rm GAS}$ (determined from the entire hot halo) below ∼1.5 keV, because $T_{\rm GAS}$ is a good measure of the total mass of the system. About 80 per cent of the sample galaxies have $T_{\rm GAS} = 0.3$–1.0 keV. For a comparison, the previous detailed study of the temperature profiles by Diehl & Statler (2008) (DS08 hereafter) included the temperature profiles of 36 ETGs with 4 yr of the *Chandra* data. We investigate the temperature profiles of hot haloes in great detail, both at large scales by examining global properties and profile trends as well as at small scales by examining the profiles within the central region of the galaxy. We compare features (e.g. peaks and dips) found in each profile to look for similarities in shape and to explore a possibility of the presence of a 'universal' profile. We then test which galaxy properties play a role in the formation of these features.

In Section 2, we show the data reduction methods and how we determine the 3D temperature profile. In Section 3, we describe six types of temperature profiles. In Section 4, we describe the common characteristics, and in Section 5, we explore the possibility of a universal temperature profile. In Section 6, we further investigate the inner temperature profile and the correlation with other galaxy properties. Finally, we summarize our results in Section 7.

2 DATA REDUCTION

2.1 Data analysis

The analysis of the archival *Chandra* data for the Chandra Galaxy Atlas (CGA) project is described in full by Kim et al. (2019a). In this paper, we will briefly describe the key steps used in this analysis. The initial step is to reprocess all the *Chandra* data with a CIAO[1] tool ***chandra_repro***, to merge multiple observations, then exclude all point sources detected by a CIAO tool ***wavdetect.*** The point-source size is determined by the point spread function (PSF).[2] Because the PSF becomes large at large off-axis angles (OAAs), we do not use observations where the target galaxy is at OAA $>$ 4 arcmin. We remove the time intervals containing high background flares with the CIAO tool ***deflare***. Because each chip will be affected differently by background flares, we apply this step per observation (specified by obsid) per chip (specified by ccdid).

This work makes use of the four adaptive spatial binning methods, which were implemented in the CGA project to characterize the spectral properties of the hot gas; (1) annulus binning (AB) with adaptively determined inner and outer radii, (2) weighted Voronoi tessellation adaptive binning (WB; Diehl & Statler 2006), (3) contour binning (CB; Sanders 2006), and (4) hybrid binning (HB; O'Sullivan, David & Vrtilek 2014). AB provides azimuthally averaged quantities, and the latter three methods provide two-dimensional spectral properties. We examine all four binning results to identify the 2D thermal structure, but only use AB and WB for quantitative measurements and model fitting, because CB and HB produce radially overlapped regions. These binning methods are controlled by pre-set S/N. We use three S/N values during the spatial binning (20, 30, and 50) to optimize the balance between resolution and statistics.

Once the adaptive spatial binning is complete, the X-ray spectra are extracted from each spatial bin, per observation per chip. The corresponding arf and rmf files are also generated, per observation per chip, in order to take account of time- and position-dependent ACIS responses. To remove background emission, we download blank sky data from the *Chandra* archive; then, for each observation, we re-project them to the same tangent plane as done in the observations. We also rescale them to match the higher energy (9–12 keV) rate, where the photons are primarily from the background (Markevitch 2003). We compared our results with those made by the local background from the off-axis, source-free region from the same observation in a few cases, and found no significant difference.

After generating source spectrum, background spectrum, arf, and rmf per observation per chip, we use a CIAO tool, ***combine_spectra***, to combine them to make a single data set per bin.[3] We also performed a joint fit by simultaneously fitting individual spectra and

[1] http://cxc.harvard.edu/ciao/

[2] http://cxc.harvard.edu/ciao/PSFs/psf_central.html

[3] This tool, *combine_spectra* with an option *method* = *sum*, makes the exposure time of the combined spectrum to be the sum of those of individual spectra. This is proper when multiple obsids are combined, but not when multiple chips (ccdid) of a given obsid are combined. In this case, we manually correct the exposure time to be the average value of multiple chips of the same obsid. Note that if *combine_spectra* is used with an option

Table 1. Early-type galaxy.

Name	T	Dist	R_e	$\log(L_K)$	Age	$\log(\sigma)$	$\log(L_{1.4})$	$\log(M)$		$\log(L_X)$		T_{GAS}	∇T_{CORE}	T_{MAX}	R_{MAX}	T_{MIN}	R_{MIN}	R_{VIR}	Type
								Total	BH	AGN	Gas								
		Mpc	kpc	$L_K\odot$	Gyr	km s^{-1}	erg s^{-1} Hz^{-1}	M$\odot$	M$\odot$	erg s^{-1}	erg s^{-1}	keV		keV	kpc	keV	kpc	Mpc	
(1)	(2)	(3)	(4)	(5)	(6)	(7)	(8)	(9)	(10)	(11)	(12)	(13)	(14)	(15)	(16)	(17)	(18)	(19)	(20)
I1262	− 5.0	130.2	7.7	11.4	–	2.37	29.5	–	–	41.0	43.2	1.30	0.05	1.72	67.9	0.93	8.5	0.92	H-bump
I1459	− 5.0	29.2	5.2	11.5	8.0	2.49	30.1	12.0	9.4	41.0	40.6	0.48	− 0.15	–	–	–	–	0.56	Neg
I1860	− 5.0	93.8	8.4	11.6	–	2.38	29.3	–	–	40.5	42.7	1.37	0.28	1.35	35.3	–	–	0.95	H-bump
I4296	− 5.0	50.8	11.9	11.7	5.2	2.53	31.8	12.4	9.1	40.9	41.0	0.88	0.06	1.17	13.8	0.78	1.5	0.76	H-bump
N0193	− 2.5	47.0	4.4	11.0	–	2.30	–	–	8.4	40.3	41.2	0.77	–	0.97	25.5	0.69	8.3	0.71	H-bump
N0315	− 4.0	69.8	12.5	11.8	6.6	2.54	31.0	–	8.9	41.5	41.0	0.64	0.06	–	–	–	–	0.65	Pos
N0383	− 3.0	63.4	6.3	11.5	–	2.46	31.4	–	8.8	40.9	41.3	1.35	0.01	1.73	64.7	0.81	2.0	0.94	H-bump
N0499	− 2.5	54.5	4.3	11.3	–	2.38	27.4	–	–	39.8	42.2	0.70	− 0.06	–	–	0.72	9.9	0.68	H-dip
N0507	− 2.0	63.8	12.9	11.6	8.1	2.44	29.5	–	–	39.7	42.9	1.32	0.03	1.34	69.6	–	–	0.93	H-bump
N0533	− 5.0	76.9	16.2	11.7	–	2.45	29.3	–	–	40.4	42.0	0.98	0.01	1.41	32.5	0.81	4.4	0.80	H-bump
N0720	− 5.0	27.7	4.8	11.3	5.4	2.38	26.6	11.4	–	39.6	40.7	0.54	− 0.55	–	–	–	–	0.60	Neg
N0741	− 5.0	70.9	13.2	11.7	–	2.46	30.8	–	8.7	40.5	41.4	0.96	0.02	1.58	30.1	0.8	4.1	0.79	H-bump
N1132	− 4.5	95.0	15.5	11.6	–	2.38	28.8	12.2	–	40.3	42.9	1.08	0.24	1.15	13.4	–	–	0.84	H-bump
N1316	− 2.0	21.5	7.6	11.7	3.2	2.35	31.9	12.2	8.2	39.8	40.7	0.60	− 0.15	—	–	–	–	0.63	Neg
N1332	− 3.0	22.9	3.0	11.2	–	2.50	27.5	11.7	9.2	39.5	40.4	0.41	− 0.11	–	–	0.56	3.1	0.52	H-dip
N1380	− 2.0	17.6	3.2	11.1	4.4	2.39	26.8	11.4	–	39.1	40.0	0.30	− 0.26	–	–	0.28	2.1	0.44	H-dip
N1387	− 3.0	20.3	3.5	11.0	–	2.23	27.3	11.3	–	36.7	40.6	0.41	− 0.30	–	–	0.35	4.2	0.52	H-dip
N1395	− 5.0	24.1	5.4	11.3	7.6	2.40	26.9	–	–	40.0	40.4	0.65	–	0.93	10.8	–	–	0.65	H-bump
N1399	− 5.0	19.9	4.7	11.4	11.5	2.53	30.0	12.6	8.9	38.9	41.5	1.21	− 0.09	1.44	22.6	0.93	0.6	0.89	D-brk
N1400	− 3.0	26.4	2.9	11.0	15.0	2.41	27.3	11.3	–	39.7	40.0	0.55	–	–	–	–	–	0.60	Pos
N1404	− 5.0	21.0	2.7	11.2	9.0	2.38	27.3	11.6	–	39.5	41.2	0.58	− 0.15	–	–	0.55	4.5	0.62	H-dip
N1407	− 5.0	28.8	8.9	11.6	7.4	2.41	28.9	12.3	9.7	39.9	41.0	0.87	− 0.19	1.29	28.9	0.76	1.9	0.76	D-brk
N1550	− 3.2	51.1	6.3	11.2	–	2.49	28.7	–	9.6	40.2	43.2	1.33	0.11	1.38	44.7	1.04	4.5	0.93	H-bump
N1553	− 2.0	18.5	5.1	11.3	4.7	2.32	–	11.5		40.1	40.5	0.41	–	–	–	–	–	0.52	Neg
N1600	− 5.0	57.4	13.5	11.6	9.7	2.54	29.4	12.2	10.2	40.2	41.5	1.43	0.15	1.48	46.4	1.03	4.3	0.97	H-bump
N1700	− 5.0	44.3	3.9	11.4	2.6	2.36	27.2	11.8	–	40.1	41.0	0.43	− 0.19	–	–	–	–	0.53	Neg
N2300	− 2.0	30.4	4.8	11.2	7.3	2.40	27.5	–	–	39.3	41.2	0.62	0.00	1.02	23.8	0.68	3.7	0.64	H-bump
N2563	− 2.0	67.8	6.4	11.4	–	2.42	27.2	–	–	39.9	41.9	1.48	0.21	1.77	21.1	–	–	0.99	H-bump
N3402	− 4.0	60.4	8.2	11.3	–	2.50	29.1	–	–	40.0	42.7	0.96	–	–	–	–	–	0.79	Irr
N3923	− 5.0	22.9	5.8	11.4	3.3	2.43	26.8	12.1	9.5	39.2	40.6	0.45	− 0.18	–	–	0.45	3.2	0.54	H-dip
N4104	− 2.0	120.0	20.0	11.8	–	–	–	–	–	40.8	42.7	1.52	0.37	1.72	27.7	–	–	1.00	H-bump
N4125	− 5.0	23.9	5.9	11.3	5.9	2.35	28.2	–	–	39.3	40.5	0.41	− 0.15	–	–	–	–	0.52	Neg
N4261	− 5.0	31.6	6.9	11.4	16.3	2.47	31.4	11.8	8.7	40.2	40.9	0.76	0.02	1.35	10.2	0.77	2.7	0.71	H-bump
N4278	− 5.0	16.1	2.6	10.9	12.0	2.40	29.1	11.4	8.0	40.3	39.4	0.30	− 0.34	–	–	0.31	1.9	0.44	H-dip
N4291	− 5.0	26.2	2.0	10.8	2.41	–	26.6	11.6	9.0	39.7	40.9	0.59	− 0.47	–	–	0.4	3.1	0.62	H-dip
N4325	0.0	110.0	10.5	11.3	–	–	–	–	–	40.4	43.1	1.00	0.01	1.08	51.2	0.83	6.8	0.81	H-bump
N4342	− 3.0	16.5	0.5	10.1	–	2.35	–	–	8.7	39.4	39.2	0.59	− 0.28	–	–	0.54	3.7	0.62	H-dip
N4374	− 5.0	18.4	5.5	11.4	12.8	2.45	30.5	12.4	9.0	40.0	40.8	0.73	− 0.12	1.31	47.1	0.61	0.7	0.69	D-brk
N4382	− 1.0	18.5	7.4	11.4	1.6	2.26	26.5	11.8	7.1	39.3	40.0	0.39	− 0.20	–	–	–	–	0.51	Neg
N4406	− 5.0	17.1	10.3	11.3	–	2.34	–	12.1	–	39.0	42.1	0.82	0.03	–	–	–	–	0.73	Pos
N4438	0.0	18.0	5.0	10.9	–	2.13	28.4	–	–	39.6	40.5	0.83	− 0.17	–	–	0.39	1.2	0.74	H-dip
N4472	− 5.0	16.3	8.2	11.6	9.6	2.46	28.8	12.5	9.4	38.9	41.3	0.95	0.02	–	–	–	–	0.79	Pos

Table 1 – *continued*

Name	T	Dist	R_e	$\log(L_K)$	Age	$\log(\sigma)$	$\log(L_{1.4})$	$\log(M)$		$\log(L_X)$		T_{GAS}	∇T_{CORE}	T_{MAX}	R_{MAX}	T_{MIN}	R_{MIN}	R_{VIR}	Type
								Total	BH	AGN	Gas								
		Mpc	kpc	$L_K\odot$	Gyr	km s^{-1}	erg s^{-1} Hz^{-1}	M$\odot$	M$\odot$	erg s^{-1}	erg s^{-1}	keV		keV	kpc	keV	kpc	Mpc	
(1)	(2)	(3)	(4)	(5)	(6)	(7)	(8)	(9)	(10)	(11)	(12)	(13)	(14)	(15)	(16)	(17)	(18)	(19)	(20)
N4477	− 2.0	16.5	3.5	10.8	11.7	2.23	26.4	–	7.6	39.0	40.0	0.33	− 0.30	–	–	0.33	2.3	0.47	H-dip
N4552	− 5.0	15.4	3.0	11.0	12.4	2.42	28.5	11.7	8.7	39.7	40.3	0.59	− 0.32	–	–	0.42	3.7	0.62	H-dip
N4555	− 5.0	91.5	13.2	11.6	–	2.52	–	–	–	39.6	41.7	1.00	0.04	1.2	19.1	0.85	4.0	0.81	H-bump
N4636	− 5.0	14.7	6.7	11.1	13.5	2.30	28.3	12.0	8.6	38.9	41.5	0.73	0.18	0.94	25.4	0.71	2.8	0.69	H-bump
N4649	− 5.0	16.8	6.2	11.5	14.1	2.50	28.0	12.1	9.7	38.7	41.2	0.86	− 0.19	–	–	0.85	1.1	0.75	H-dip
N4782	− 5.0	60.0	4.4	11.8	–	2.53	31.5	–	–	40.2	41.4	1.15	0.13	1.58	55.2	0.83	8.5	0.87	H-bump
N5044	− 5.0	31.2	3.9	11.2	14.2	2.37	28.6	–	–	39.9	42.4	0.91	0.01	1.33	53.9	0.93	5.4	0.77	H-bump
N5129	− 5.0	103.0	14.3	11.6	–	2.42	–	–	–	40.5	42.6	0.81	0.19	1.04	19.5	–	–	0.73	H-bump
N5171	− 3.0	100.0	12.4	11.3	–	–	–	–	–	40.8	41.8	0.86	–	1.27	15.7	–	–	0.75	H-bump
N5813	− 5.0	32.2	8.3	11.4	16.6	2.35	28.3	12.1	8.9	39.6	41.9	0.70	–	–	–	–	–	0.68	Irr
N5846	− 5.0	24.9	7.2	11.3	14.2	2.37	28.2	12.3	9.0	39.4	41.7	0.72	− 0.06	1.08	29.5	0.71	2.2	0.69	D-brk
N6338	− 2.0	123.0	17.1	11.7	–	2.54	30.0	–	–	41.4	43.4	1.97	0.05	2.41	64.8	1.34	8.7	1.14	H-bump
N6482	− 5.0	58.4	6.3	11.5	11.4	2.50	27.8	11.8		40.6	42.2	0.74	− 0.06	–	–	–	–	0.70	Neg
N6861	− 3.0	28.1	3.1	11.1	–	2.61	–	11.9	9.3	39.7	41.3	1.08	0.01	1.31	6.9	0.82	2.5	0.84	H-bump
N6868	− 5.0	26.8	3.9	11.2	9.2	2.46	–	–	–	39.9	41.3	0.69	0.02	–	–	–	–	0.67	Pos
N7618	− 5.0	74.0	7.8	11.4	–	2.47	29.4	–	–	40.5	42.3	0.80	–	–	–	–	–	0.72	Irr
N7619	− 5.0	53.0	8.8	11.6	15.4	2.48	28.8	—	9.4	39.9	41.9	0.81	0.06	1.04	56.1	–	–	0.73	H-bump
N7626	− 5.0	56.0	12.0	11.6	13.9	2.40	30.4	12.1	8.6	40.5	41.2	0.79	0.17	–	–	–	–	0.72	Pos

Note. 1. Galaxy name.

2. Morphological type from RC3.

3. Distance in Mpc taken mostly from SBF measurements, in order of preference, Tonry et al. (2001), Jensen et al. (2003), Cappellari et al. (2011), Lauer et al. (2007), and Tully et al. (2013). If not available, we take the distance from NED in http://ned.ipac.caltech.edu.

4. Effective radius (R_e) in kpc, taken from Atlas3D (Cappellari et al. 2013), RC3, and 2MASS following the prescription in Cappellari et al. (2011), Lauer et al. (2007), Blakeslee et al. (2001), and NSA in http://www.nsatlas.org.

5. K-band luminosity. K mag is taken from 2MASS (via NED) and converted with $M_K\odot = 3.28$ mag.

6. Stellar age assuming a single stellar population taken from, in order of preference, Thomas et al. (2005), Terlevich & Forbes (2002), Trager et al. (2000), Kuntschner et al. (2010), Annibali et al. (2010), Denicolo et al. (2005), and S'anchez-Bl'azquez et al. (2006).

7. Stellar velocity dispersion taken from Thomas et al. (2005), Terlevich & Forbes (2002), Blakeslee et al. (2001), Prugniel (1996), Gültekin et al. (2009), and Hyperleda in http://leda.univ-lyon1.fr.

8. Radio luminosity in erg s^{-1} Hz^{-1} at 1.4 GHz, primarily taken from the collection of Brown et al. (2011) and supplemented by the NVSS by Condon et al. (1998).

9. Total mass inside $5R_e$, primarily taken from the GC kinematics by Alabi et al. (2017) and supplemented by scaling from the mass of GC system by Kim et al. (2019b).

10. Mass of supermassive black hole taken from Kormendy & Ho (2013), Gaspari et al. (2019), and Saglia et al. (2016).

11. X-ray luminosity in 0.3–8 keV of the central source (see Section 4).

12. X-ray luminosity in 0.3–8 keV of the hot gas from Kim et al. (2019a). For galaxies with extended haloes, $L_{X,GAS}$ was measured from the entire hot halo with the *ROSAT* or *XMM–Newton* data.

13. Temperature of the hot gas from Kim et al. (2019a).

14. Inner temperature gradient measured at $0.15R_e$ (see Section 6).

15. Temperature at the peak of the T-profile bump.

16. Galacto-centric distance at the peak of the T-profile bump.

17. Temperature at the bottom of the T-profile dip for the hybrid-dip and double-break types, or at the inner break for the hybrid-bump type.

18. Galacto-centric distance at the bottom of the T-profile dip for the hybrid-dip and double-break types, or at the inner break for the hybrid-bump type.

19. Virial radius in Mpc calculated by $0.81 \times T_{GAS}{}^{0.5}$ with T_{GAS} from Col. (13).

20. Temperature profile type determined in this work.

found no significant difference. We primarily use a two-component emission model, APEC, for hot gas, and power law for undetected LMXBs. We fix the power-law index to be 1.7, which is appropriate for the hard spectra of LMXBs (e.g. Boroson, Kim & Fabbiano 2011), and $N_{\rm H}$ to be the Galactic H I column density (Dickey & Lockman 1990). We also fix the metal abundance to be solar at GRSA (Grevesse & Sauval 1998). Although the abundance is known to vary from a few tenth to a few times solar inside the hot ISM, the hot gas temperatures do not significantly depend on the abundance (e.g. see Kim & Pellegrini 2012).

2.2 3D temperature profiles

To adequately describe the 3D gas properties, we parametrize the 3D temperature and density profiles and find the best-fitting parameters by projecting the 3D models and fitting them to the projected emissivity and projected temperature profiles. For temperature models, we use two models from Gastaldello et al. (2007), smoothly joined power laws and power laws mediated by an exponential. We also use one detailed by Vikhlinin et al. (2006), which has more parameters to fit, particularly for cooling cores and T peaks at $r \sim 0.1\ r_{200}$, often seen in typical clusters. With the temperature profiles showing a large variation in shape and structure, using all three models gives us the flexibility required to describe the various observed temperature profiles reasonably well. We apply two different initial values for each model before fitting to improve the ability of the models to converge fast for complex projected temperature profiles.

To compare with the projected T profile, we need to parametrize the density profile to calculate the emissivity. For density models, we use a single and double β model (e.g. Sarazin & Bahcall 1977) and one detailed by Vikhlinin et al. (2006), which has more parameters to fit, particularly for cooling cores and steep declining outskirts at large radii.

Since the gas temperature in ETGs is around 1 keV, the X-ray emission is dominated by emission lines over the thermal bremsstrahlung continuum. In this case, the temperature can be mainly determined by the energy at the peak intensity, and this peak energy is linearly proportional to the plasma temperature in a log scale (see fig. 2 in Vikhlinin 2006). Following Vikhlinin (2006), we estimate a projected temperature and emissivity from each model in a given spatial bin and compare with observed values to determine the best-fitting model parameters. For the profile fitting with Sherpa,[4] we proceed as follows. For each 3D density model $n(r)$, we define a 2D projected surface density profile through the integral function[5]

$$S(R) = \int_R^\infty n(r)^2 \frac{r}{\sqrt{r^2 - R^2}}\,{\rm d}r,$$

and fit the observed surface brightness profiles. We compare our best-fitting models using a χ^2 method to select which model gives the best fit to the data. If multiple models are similarly acceptable, we select the simplest model with the smallest number of parameters. Then, we define the 2D projected temperature profile, $t(R)$, through the best-fitting 3D density profile and the 3D temperature model, $T(r)$, using the integral function

$$\log t\ (R) = \frac{\int_R^\infty n(r)^2\ \log T\ (r)\ \frac{r}{\sqrt{r^2 - R^2}}{\rm d}r}{\int_R^\infty n(r)^2\ \frac{r}{\sqrt{r^2 - R^2}}{\rm d}r}$$

and fit the observed 2D projected temperature profiles. Again, we compare our best-fitting models using a χ^2 method to select which model gives the best fit to the data. We note that the density and temperature profiles parametrized by the corresponding models are useful, but not the models themselves as long as the models reproduce the observed profiles. The parametrized profiles can be used to measure the entropy, pressure, and mass profiles and we will present them with proper abundance measurements in the next paper. In this paper, we focus on the shape of the temperature profile.

3 TEMPERATURE PROFILE TYPES

The isothermal hot ISM may be the simplest case, but we do not see such a case in a single galaxy. Instead, we always find radial variations with positive or negative gradients. Some galaxies have monotonically decreasing or increasing temperature profiles, while others show one or more breaks with bumps and/or dips in their temperature profiles. We categorize the observed temperature profiles in our sample into six types, namely hybrid-bump (rising at small radii and falling at large radii), hybrid-dip (falling at small radii and rising at large radii), double-break (falling at small radii, rising at intermediate radii, and falling again at large radii), positive (rising all the way), negative (falling all the way), and irregular. DS08 adopted four different types (hybrid-bump, positive, negative, and quasi-isothermal). We have added three new types (hybrid-dip, double-break, and irregular), but excluded the isothermal type because we found no obvious isothermal case. We show an example of each profile type in Fig. 1. For the entire sample of 60 ETGs, we present the observed temperature profiles and the best-fitting models in Appendix A.

To determine the type, we have examined the temperature profiles made in four different spatial binning methods and three different s/n values and corresponding 2D temperature maps. In particular, the 2D binning methods retain the spatial information, which provides 2D gas distribution and its temperature. This allows gas structure and/or any asymmetry in the haloes to be identified. Non-spherically symmetric gas distributions manifest in the projected temperature profiles as vertical (temperature) scatter, due to the range of gas temperatures at the same radii. In this work, we intend to determine the shape of the global temperature profile and use the azimuthally averaged radial profiles. The azimuthal variation (e.g. analysing different pie sectors) will be addressed in future work. If X-ray bright nearby galaxies exist within the X-ray halo of the target galaxy, we exclude the corresponding 2D spatial bins from the profile before fitting.

3.1 Hybrid-bump

The temperature profiles in the hybrid-bump type all have a temperature peak in the middle of the observable radius range. The temperature gradient is positive inside the peak and negative outside the peak. This is most common, with 26 (or 43 per cent) out of 60 belonging to this type. In our sample, the peak with $T_{\rm MAX} = 1$–2 keV lies at $R_{\rm MAX} = 10$–70 kpc, or a few hundredth $R_{\rm VIR}$ (see Table 2 for $T_{\rm MAX}$ and $R_{\rm MAX}$ and Sections 4 and 5 for more discussions). This type is similar to a typical profile of groups and clusters, except

method = avg to get an average exposure time, the combined arf is the sum of individual files, which is not applicable.

[4] http://cxc.harvard.edu/sherpa/

[5] Integrals are performed making use of the QUAD function from the python package, scipy.integrate.

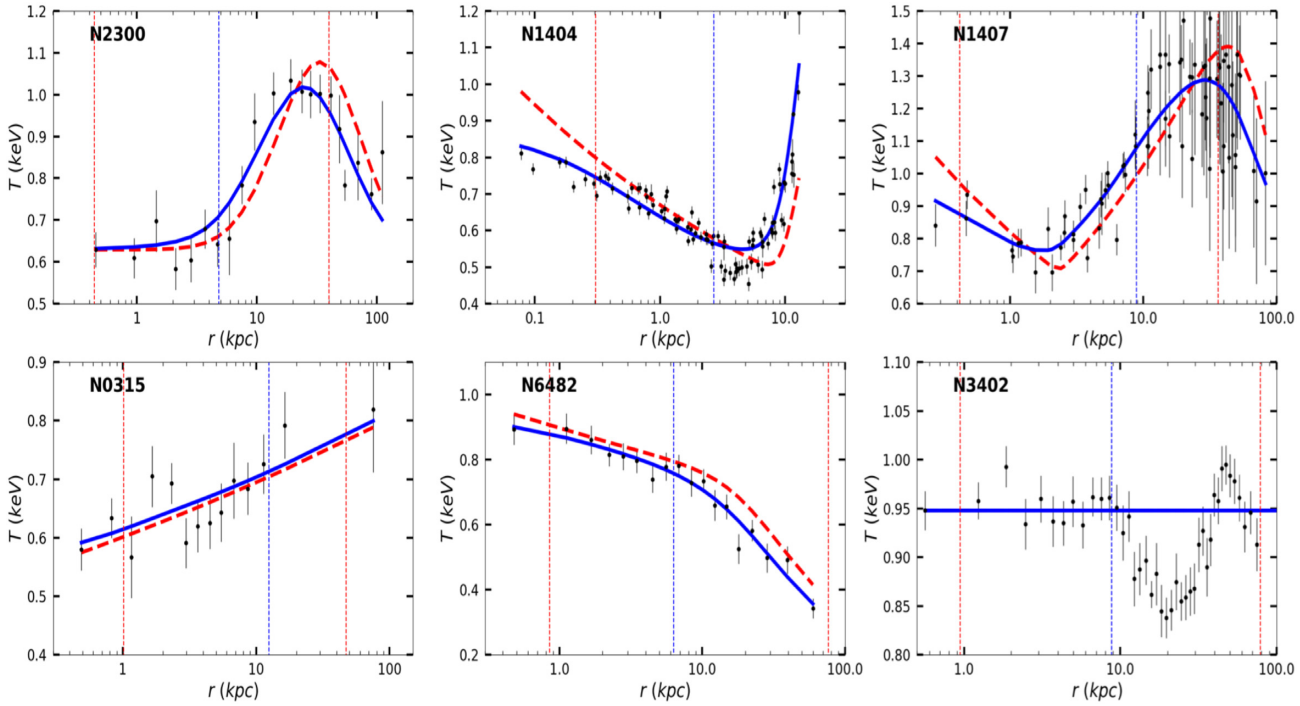

Figure 1. Examples of six different temperature profile types. All the galaxies in our sample are shown in Appendix A. From left to right and top to bottom: hybrid-bump (rising at small radii and falling at large radii), hybrid-dip (falling at small radii and rising at large radii), double-break (a profile containing both a dip and peak), positive (monotonically rising), negative (monotonically falling), and irregular. The data points in black are fitted with projected temperature profiles in blue with the 3D model shown in a red dashed line. The inner red vertical line indicates $r = 3'$ where the AGN could affect the temperature measurement, and the outer red line indicates the maximum radius where the hot gas emission is reliably detected with an azimuthal coverage larger than 95 per cent. The blue vertical line is at one effective radius.

that $R_{\rm MAX}$ is smaller than that found for clusters where the peak is at $r \sim 0.1\ R_{\rm VIR}$, or $r \sim$ 100–200 kpc (for systems with $T =$ 2–10 keV).

The profiles in this type can be separated further into two subsamples based on their inner slope change. We find that 17 out of the 26 hybrid-bump profiles show a flattening at small radii. We compare two examples in Fig. 2. In NGC 5129 (left-hand panel), the temperature profiles show a constant gradient at small radii ($r < R_{\rm MAX}$). In NGC 533 (right-hand panel), the temperature increases slowly at small radii, rapidly increases at intermediate radii, and then decreases at large radii. The galacto-centric distance of the inner break is at $R_{\rm BREAK} \sim 5 \pm 2$ kpc (see Table 2 and Sections 4 and 5). For a few distant galaxies (e.g. NGC 4104 at 120 Mpc), this radius falls within a few arcsec from the centre such that the inner break would not be properly recognized due to the possible contamination of AGNs. Therefore, the presence of the inner break may be more frequent than we could identify in this work.

3.2 Hybrid-dip

This is the second largest with 13 galaxies or 22 per cent in our sample. Opposite to the hybrid-bump type, the profiles in this hybrid-dip type have a negative temperature gradient at $r < R_{\rm MIN}$ and a positive gradient at $r > R_{\rm MIN}$ with a single temperature minimum at $r = R_{\rm MIN}$ in the middle of the observable radius range. In this type, the dip is found at $T_{\rm MIN} = 0.49 \pm 0.16$ keV and $R_{\rm MIN} = 3.4 \pm 2.1$ kpc, which is considerably cooler and smaller than $T_{\rm MAX}$ and $R_{\rm MAX}$ of the hybrid-bump type (see Table 2 and Section 4 for more discussions). NGC 499, which is likely a small group, has the largest $R_{\rm MIN}$ (9.9 kpc) in this type.

In terms of the temperature gradient at $r > R_{\rm MIN}$, there may be two cases. Some galaxies (e.g. NGC 1332 and NGC 4278) have a slope (∼0.3; see Section 4), which is similar to that of the hybrid-bump type, while others (e.g. NGC 499 and NGC 1404) have a considerably steeper slope. The latter case is a non-BCG galaxy (or a subgroup) embedded in the hotter gas (see Appendix A for individual galaxies and Section 5 for more discussions).

3.3 Double-break

There are four galaxies with double-breaks in their temperature profile, i.e. a combination of hybrid-bump and hybrid-dip profile types. They show a dip at small radii and a peak at larger radii. The temperature gradient is negative, positive, then negative from the centre to the outskirts. There is no case with an opposite combination, i.e. a peak in small radii and a dip in large radii.

3.4 Positive

There are six galaxies with a positive gradient with no change in the gradient sign within the observable radius range. The temperature increases monotonically from the centre to the outskirts. Most galaxies in this type may be similar to the hybrid-bump type, but we may not observe the outer temperature drop, because they are embedded inside the hotter groups/clusters (e.g. NGC 4472 in the Virgo cluster) and/or the outer region is not observed due to the limited ACIS field of view (fov; see more discussion in Section 5).

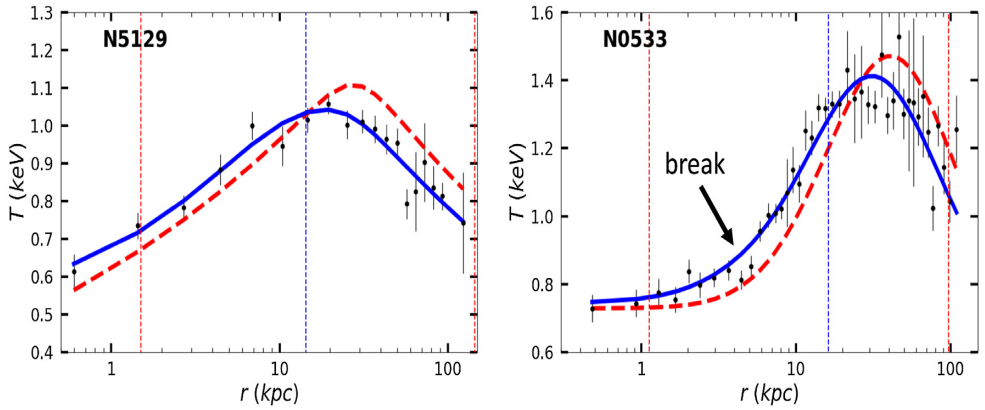

Figure 2. Hybrid-bump temperature profiles, (left) one that shows a peak with one break and (right) another that shows a second break in the slope at small radii, $r < R_{MAX}$. All the symbols and colours are the same as in Fig. 1.

3.5 Negative

There are eight galaxies with a negative gradient with no change in the gradient sign within the observable radius range. Opposite to the positive case, the temperature decreases monotonically from the centre to the outskirts. Some galaxies (e.g. NGC 4382) in this type may be similar to the hybrid-dip type, but we cannot measure the outer region where the temperature slope changes the sign to be positive, because the X-ray emission is too faint (see more discussion in Section 5). However, NGC 6482 is the most obvious example of this negative type with a continuously decreasing T in a wide radius range (from a few kpc to ∼60 kpc).

3.6 Irregular

There are three cases where the T profile does not fit any type listed above. A good example is NGC 3402 (=NGC 3411), where cooler gas forms a shell-like structure at 20–40 kpc, which is surrounded by inner and outer hotter gas with a relatively constant temperature (∼1 keV) (O'Sullivan et al. 2007). Some profiles in the hybrid-dip type may look similar to these cases with a cooler ring, but in general, the slope change in the hybrid-dip type is smoother in a wider radius range than those of NGC 3402. Because of the irregular nature of the profile, the best-fitting line in Appendix A does not represent reality.

The second case is NGC 5813, where the hot gas morphology exhibits three sets of nested co-aligned cavities and shocks (Randall et al. 2011 and 2015). Consequently, the temperature profile shows multiple peaks (at ∼1 kpc and ∼10 kpc) and dips (at ∼3 kpc and ∼20 kpc). Another peak at $r \sim 50$ kpc (similar to the peak in hybrid-bump) is identified by the *XMM–Newton* data (Islam et al., in preparation). Again, the best-fitting line in Appendix A does not represent reality.

The last case of the irregular type is NGC 7618, which is a well-known sloshing system (Kraft et al. 2006; Roediger et al. 2012). The pronounced spiral-like features, likely caused by UGC 12 491, redistribute the cooler gas, resulting in the complex temperature profile with a positive gradient at $r < \sim 2$ kpc, a negative gradient at $r = 2$–30 kpc, then a positive gradient at $r < \sim 30$ kpc. The shape may look like a reversed double-break type, but the temperature is likely to drop again at the outskirts, making it different from the typical double-break type.

In summary, we identified 26 hybrid-bump, 13 hybrid-dip, 4 double-break, 6 positive, and 8 negative types. The remaining three are irregular for their specific reason.

4 CHARACTERISTICS OF TEMPERATURE PROFILES

We find that ETGs in our sample show complex thermal structures. None of them can be described as isothermal. While some (23 per cent) have a single temperature gradient (positive and negative types), the majority of ETGs have multiple gradients with one or two breaks (72 per cent), having both positive and negative gradients in their radial profiles (hybrid-bump, hybrid-dip, and double-break types).

4.1 The temperature peaks and dips in the *R–T* plane

To examine the observed characteristics of the temperature profiles in our sample quantitatively, we compare the bumps and dips of the profiles in terms of their temperature and galacto-centric distance. In the left-hand panel of Fig. 3, we plot the temperatures of the peaks (red upward triangles) of the hybrid-bump and the dips (blue downward triangles) of the hybrid-dip types against their radii. In this *R–T* plane, the peaks and dips are clustered in two distinct locations: the dips are found at the lower left corner and the peaks at the upper right corner. In other words, the peaks are found at higher T and larger R than the dips. Quantitatively, the dip of the hybrid-dip type has a T_{MIN} (∼0.5 keV), which is always lower than the T_{MAX} (∼1.4 keV) of the peak in the hybrid-bump type with no exception. The mean and standard deviation of the dips and peaks are listed in Table 2 and marked in Fig. 3 by blue and red crosses, respectively. The difference between the two mean temperatures is significant at the 2.5σ confidence level. The galacto-centric distance of the dip ($R_{MIN} \sim 3.4$ kpc) is smaller than that of the peak ($R_{MAX} \sim 35$ kpc) with a small number of exceptions. In one case of the hybrid-dip type, the dip is at ∼10 kpc ($R_{MIN} = 9.9$ kpc for NGC 499), and in one case of the hybrid-bump type, the peak is inside 10 kpc ($R_{MAX} = 7$ kpc for NGC 6861). The difference between the two mean radii is significant at the 1.6σ level. Based on the two-dimensional Kolmogorov–Smirnov test (Fasano & Franceschini 1987), the null hypothesis probability that two subsamples are originated from the same parent population is 4.3×10^{-8}, suggesting that the dip and peak are two distinct characteristics.

There are a small number (four) of interesting double-break cases where the temperature profile has both a peak and a dip. We mark them in the left-hand panel of Fig. 3 by the green upward and downward triangles, respectively. In all the four cases, we

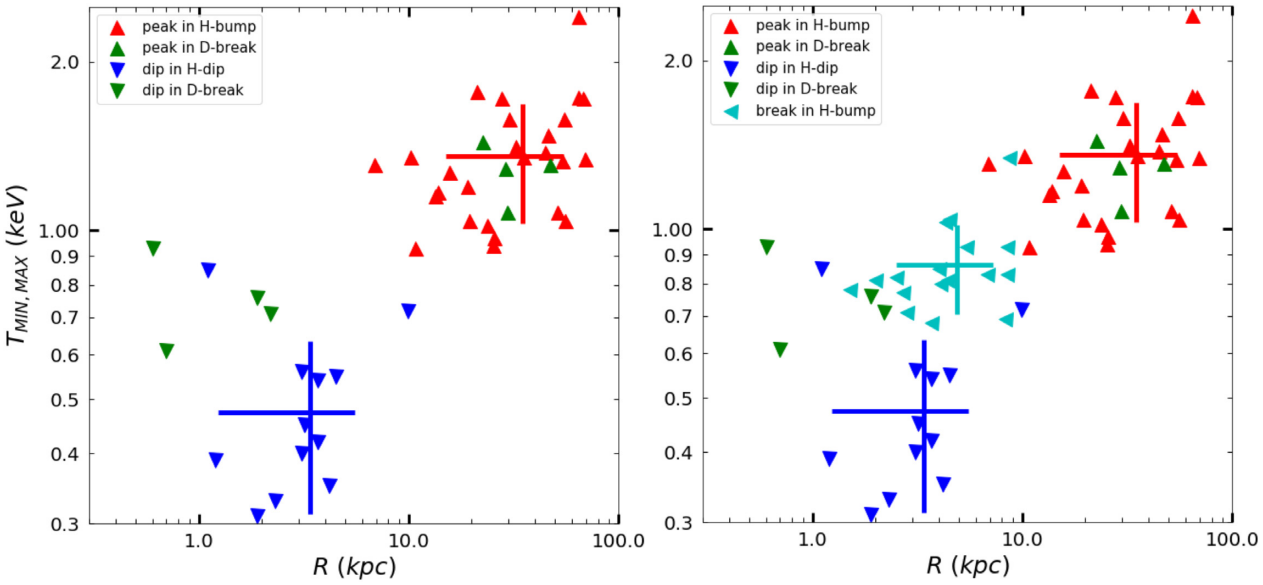

Figure 3. Comparison of the peaks and dips of the temperature profiles in terms of their temperature and galacto-centric distance. The crossbars indicate the group mean and standard deviation of individual profile types, marked by the same colour.

find $R_{MAX} > R_{MIN}$ and $T_{MAX} > T_{MIN}$. The peak and dip of this type are similar in their radius and temperature to the peak of the hybrid-bump type and the dip of the hybrid-dip types, respectively, suggesting that they, albeit rare, can provide important clues on possible connections between the hybrid-dip and hybrid-bump types (see Section 5).

As described in Section 3.1 and Fig. 2, 17 of 26 galaxies of the hybrid-bump type have an inner temperature break with a slope being flatter at small radii ($r < R_{BREAK}$). These 17 breaks of the hybrid-bump type are plotted in the right-hand panel of Fig. 3 (left-pointing cyan triangles). The mean and standard deviation of these breaks are marked by a cyan cross (see also Table 2). Their galacto-centric distances are similar to those of the dips of the hybrid-dip type. Their temperatures are slightly higher than those of the dips of the hybrid-dip type.

The similar location of the inner break of the hybrid-bump type and the dip of the hybrid-dip and double-break types suggests that they may be linked, possibly by a similar origin. To further investigate this possibility, we plot the dips, peaks, and breaks in a rescaled *R*–*T* plane. In Fig. 4, T_{MIN}, T_{BREAK}, and T_{MAX} are rescaled by T_{GAS} for each galaxy, which is the gas temperature determined by a single spectral fitting (with the spectra extracted from the entire region). T_{GAS} is taken from the Chandra Galaxy Atlas (see Kim et al. 2019a, and references therein). The galacto-centric distance is also scaled by the viral radius (R_{VIR}), which is determined by the scaling relation given by Helsdon & Ponman (2003),

$$R_{VIR} = 0.81(T_{GAS}/1\mathrm{keV})^{1/2}\mathrm{Mpc}.$$

We list R_{VIR} of individual galaxies in Table 1. Remarkably, the inner breaks and the dips are statistically identical in this scaled *R*–*T* plane. This strongly suggests that the hybrid-bump, double-break, and hybrid-dip types are related. Furthermore, given that the lack of a temperature peak in the hybrid-dip type may be caused by the observational limitation and/or selection effects, these three types may share the common temperature profile shape (see Section 5). We also find that the scatters in *R* and *T* of the peak and the dip/break are comparable, typically 0.1–0.2 dex.

The thin lines in Fig. 4 connect the inner break and the peak for the 17 hybrid-bump-type galaxies and the dip and the peak for the 4 double-break-type galaxies. The slopes are similar. The mean slope is 0.3 ± 0.1 for these 21 galaxies, again suggesting common characteristics in their temperature profile. As noted in Section 3.2, the slope of hybrid-dip-type galaxies at $r > R_{MIN}$ varies widely, because some galaxies are embedded inside the hotter gas of the groups and clusters.

In summary, we find an obvious break of the temperature gradient in the three-quarters of our sample. Of these, we identify a peak at the outer region in 30 ETGs, and a dip (or an inner break) at the inner region in 35 ETGs. We find two breaks in 21 ETGs. The temperature peaks are found at $r \sim 35$ kpc (or $\sim$0.04 R_{VIR}) on average, and the temperature dips/breaks are at $r \sim 4$ kpc (or $\sim$0.006 R_{VIR}) on average. The slope between the peak and the dip (or the inner break) is $\sim$0.3.

4.2 Different types in the $L_{X,GAS}$–T_{GAS} plane

To understand the characteristics of ETGs in individual temperature profile types better, we look at the global properties of the hot gas. Fig. 5 shows their $L_{X,GAS}$–T_{GAS} relations. $L_{X,GAS}$ is the X-ray luminosity in 0.3–8 keV from the entire hot ISM and T_{GAS} is the gas temperature determined by the spectra extracted from the entire region or similar to the luminosity-weighted mean temperature in a logarithmic scale. We take $L_{X,GAS}$ and T_{GAS} from the Chandra Galaxy Atlas (see Kim et al. 2019a, and references therein). $L_{X,GAS}$ was measured primarily with the *Chandra* data. For galaxies with extended haloes, *ROSAT* or *XMM–Newton* results were taken from the literature. While the entire sample shows a tight positive correlation as previously known (e.g. Boroson et al. 2011; Kim & Fabbiano 2015; Goulding et al. 2016; Babyk et al. 2018), the locations of different profile types in this *L*–*T* plane convey useful information. On the left-hand panel, we compare the hybrid-bump and hybrid-dip types. The hybrid-bump-type galaxies (red upward triangles) are preferentially found in the upper right corner and the hybrid-dip-type galaxies (blue downward triangles) in the lower

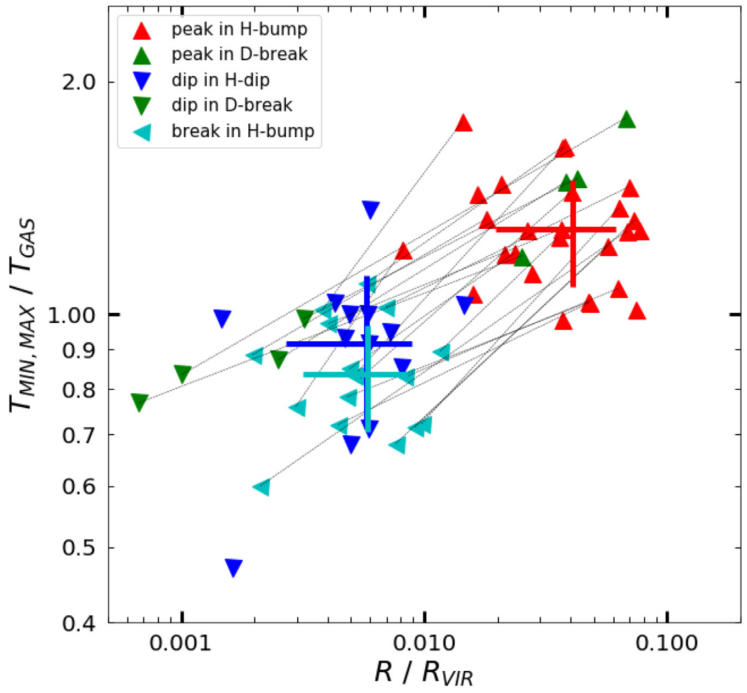

Figure 4. Same as Fig. 3, but R and T are rescaled in a log scale by $R_{\rm VIR}$ and $T_{\rm GAS}$. The thin lines connect the peak and the inner break (or the dip) for 21 individual galaxies. The mean slope is 0.3 ± 0.1.

Table 2. Means and standard deviations of the peaks and dips in individual profile types.

	N	$<T_{\rm MIN}>$	σ	$<T_{\rm MAX}>$	σ	$<R_{\rm MIN}>$	σ	$<R_{\rm MAX}>$	σ
Hybrid-bump	26	–	–	1.4	0.33	–	–	34.8	19.7
Hybrid-Dip	13	0.47	0.16	–	–	3.4	2.1	–	–
Double-break	4	0.75	0.12	1.3	0.13	1.4	0.7	32.0	9.1
	N	$<T_{\rm BREAK}>$	σ			$<R_{\rm BREAK}>$	σ		
Hybrid-bump	17	0.86	0.16	–	–	4.9	2.4	–	–

Note. $R_{\rm MAX}$ and $T_{\rm MAX}$ are the galacto-centric distance and temperature at the peak of the T bump, respectively.
$R_{\rm MIN}$ and $T_{\rm MIN}$ are the galacto-centric distance and temperature at the bottom of the T dip, respectively.
$R_{\rm BREAK}$ and $T_{\rm BREAK}$ are the galacto-centric distance and temperature at the inner break of the 17 hybrid-bump-type galaxies, respectively.

left corner, i.e. the hybrid-bump-type galaxies host hotter and more luminous gas than the hybrid-dip-type galaxies. The means and standard deviations of the subsamples are marked by crossbars with the same colours as the data points in Fig. 5 (see also Table 3). Based on the two-dimensional Kolmogorov–Smirnov test (Fasano & Franceschini 1987), the probability that two subsamples are originated from the same parent population is 2.7×10^{-5}, indicating they are significantly different at the 4σ level.

Also plotted in the left-hand panel of Fig. 5 is the double-break type (green diamonds). Its sample mean and deviation are marked by the green cross. They lie at the lower end of the hybrid-bump type.

On the right-hand panel of Fig. 5, we show the other three types: positive, negative, and irregular. For a comparison, the two crossbars from the left-hand panel are overplotted here. The negative type is found in the lower left corner, which is similar to the hybrid-dip. One exception is NGC 6482, which is comparable to the hybrid-bump. On the other hand, the positive-type galaxies host hotter and more luminous gas than the negative-type galaxies (and hybrid-dip), but they are not as hot/luminous as the typical hybrid-bump type. One exception is NGC 1400, which is comparable with the hybrid-dip.

In summary, the hottest and most luminous galaxies tend to be hybrid-bump, i.e. galaxies with a peak in their temperature profile. On the other hand, the coolest and least luminous galaxies tend to hybrid-dip or negative types, i.e. galaxies with a negative T gradient in the inner region. The double-break and positive types seem to bridge the gap between the hybrid-bump and hybrid-dip types, being at intermediate temperature and luminosity. We note that given the selection effect of our sample, the hybrid-dip and negative types are likely underrepresented because they are X-ray faint galaxies (see Section 5).

5 IS THERE A UNIVERSAL TEMPERATURE PROFILE?

As described in Section 3, the most common type is hybrid-bump. Together with the double-break type, they comprise 50 per cent of our sample (30 out of 60 galaxies). The main characteristic

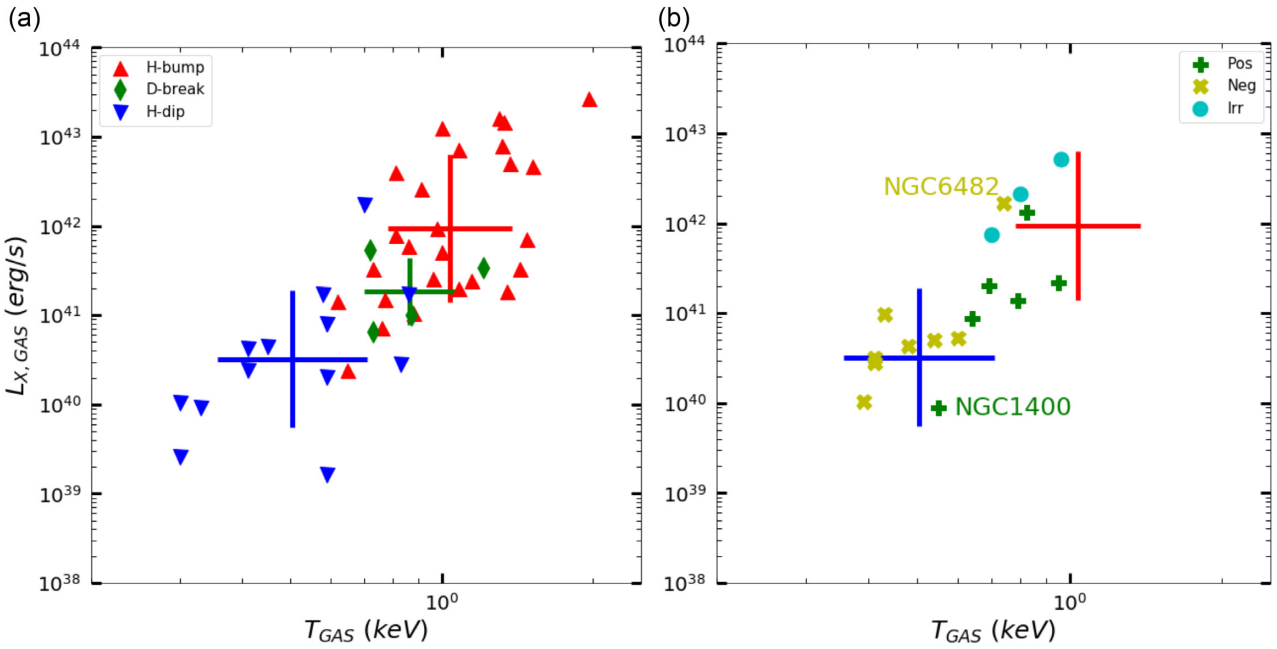

Figure 5. Comparison of the different temperature profile types in terms of their gas temperature (T_{GAS}) and luminosity ($L_{X,GAS}$). (a) The hybrid-bump type (red upward triangles) and hybrid-dip type (blue downward triangles) are seen in two separate locations. The double-break type (green diamonds) falls in the middle. The crossbars with the same colours indicate the mean and standard deviation of each type. (b) The other three types are compared. The red and blue crossbars are the same as in (a).

Table 3. Means and standard deviations of $L_{X,GAS}$ and T_{GAS}.

	N	$<\log(L_{X,GAS})>$	σ	$<T_{GAS}>$	σ
Hybrid-bump	26	41.97	0.83	1.04	0.34
Hybrid-dip	13	40.61	0.82	0.52	0.21
Double-break	4	41.27	0.37	0.86	0.20
Positive	6	41.15	0.68	0.74	0.14
Negative	8	40.78	0.60	0.49	0.11
Irregular	3	42.30	0.40	0.82	0.13

feature in their temperature profiles is that the temperature peaks at R_{MAX} and decreases both inward and outward from the peak, i.e. the temperature gradient is positive between R_{MIN} (or R_{BREAK}) and R_{MAX} and negative in the outskirts ($r > R_{MAX}$). At smaller radii (at $r < R_{MIN}$ or $r < R_{BREAK}$), the temperature gradient (1) remains constant (positive) in 9 out of 26 hybrid-bump-type galaxies, (2) breaks at R_{BREAK} (becoming flatter, close to 0) in 17 of 26 hybrid-bump-type galaxies, or (3) changes its sign to negative in 4 double-break-type galaxies.

Motivated by these characteristic temperature profiles (and the reasons described below for other types), we further explore the possibility of a *universal* temperature profile of the hot ISM in ETGs. To test whether the T profiles can be adequately scaled to identify the universal profile, in Fig. 6 (left-hand panel), we plot the temperature of all galaxies in the hybrid-bump and double-break types. The temperature is scaled by T_{MAX} (in Fig. 3) and the radius is scaled by the viral radius (R_{VIR}). Once scaled properly, the temperature profile follows a common shape qualitatively as well as quantitatively in the full radius range except in the inner region ($r < R_{MIN}$). The temperature peak at $\sim$0.04 R_{VIR}, the positive gradient with a slope of $\sim$0.3 ($\pm$ 0.1) at $R_{MIN} < r < R_{MAX}$, and the negative gradient with a relatively steeper slope of $\sim$0.5 (loosely defined, though) at $r > R_{MAX}$ are identifiable. The scatter is large in the inner region due to a wide range of the core T gradients (see Section 6). In the right-hand panel of Fig. 6, we show a schematic diagram of this temperature profile shape, indicating the bump, the dip, or the inner break and the slope of 0.3 between R_{MIN} (or R_{BREAK}) and R_{MAX}. The outer slope (at $r > R_{MAX}$) will be measured more reliably in the next paper with additional *XMM–Newton* archival data.

The second most popular type is hybrid-dip. In Section 4.1 and Fig. 4, we demonstrate that when properly scaled, T_{MIN} and R_{MIN} of this type are close to T_{BREAK} and R_{BREAK} of the hybrid-bump type and T_{MIN} and R_{MIN} of the double-break type, suggesting that this type may follow the universal profile (that of the double-break type) in Fig. 6. The only difference is that this hybrid-dip type does not have a temperature peak and a drop after the peak, but continuously increases to the observable radius limit. The lack of the peak may be caused by observational limitations and selection effects such that we may not see the ISM temperature declining at large radii. We consider the following three possible reasons. First, the hybrid-dip type consists primarily of hot gas-poor ETGs (see Fig. 5). Because of their small amount of hot gas, their X-ray emission is not detected at large radii. This type might be similar to the double-break if the hot gas could be detected in the outer region. NGC 1332, NGC 3923, and NGC 4278 are good examples as their hot gas is detected only out to $r \sim 20$ kpc. Secondly, some of the hybrid-dip-type galaxies are inside groups or clusters, i.e. they are satellite galaxies embedded in hotter IGM/intracluster medium (ICM). In this case, the X-ray emission from the outer region of this satellite galaxy is dominated by the hotter gas such that the temperature at large radii remains high. Again, this system might be similar to the double-break type if the hot ISM could be separated from the hotter IGM/ICM. NGC 1380, NGC 1387, NGC 1404 (inside the Fornax cluster centred on NGC 1399), NGC 499 (a subgroup possibly merging with the NGC 507 group), NGC 4552, and NGC 4649 (inside the Virgo cluster) are such examples. One of the distinct characteristics of these galaxies is the steeper positive T gradients at $r > R_{MIN}$ than

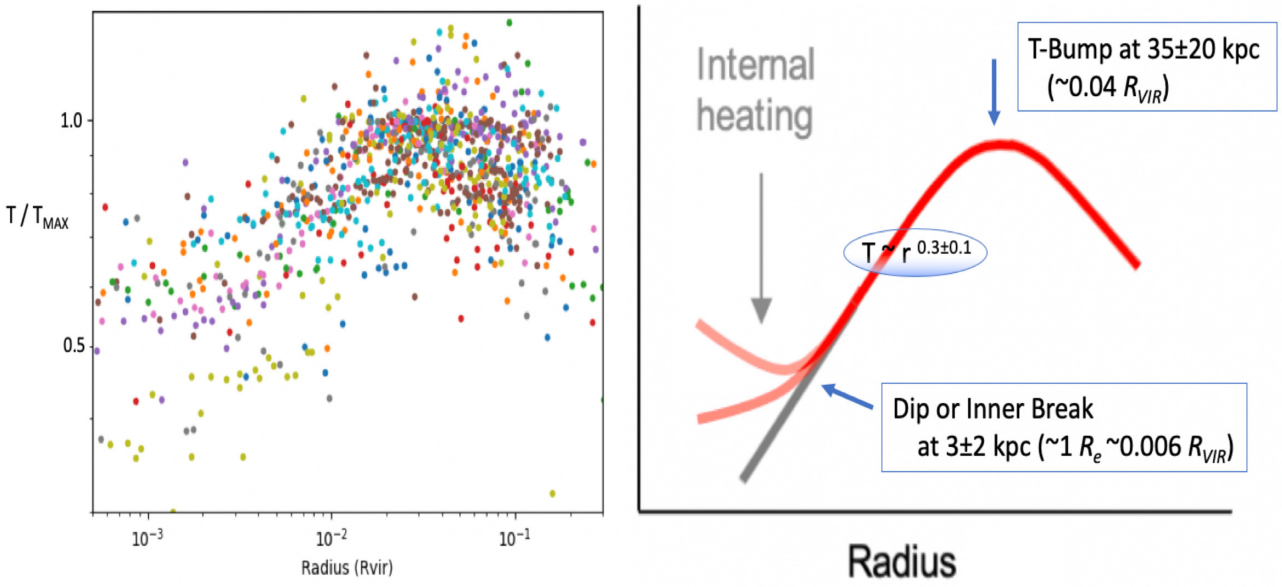

Figure 6. Left: Temperature (scaled by $T_{\rm MAX}$) against radius (scaled by $R_{\rm VIR}$) for all galaxies in the hybrid-bump and double-break types. Right: A schematic diagram of the proposed 'universal' temperature profile.

the other galaxies in the hybrid-dip type (see Appendix A). Thirdly, the detector fov is not large enough and the hot gas properties in the outer region are not well constrained. NGC 4342 is an example. The maximum radius where the hot gas emission is reliably detected with an azimuthal coverage larger than 95 per cent is 20 kpc (Kim et al. 2019a). See the vertical line in Appendix A, which indicates this limiting radius. Adding the hybrid-dip type, we can apply the universal temperature profile to 43 out of 60 ETGs or 72 per cent of our sample.

To illustrate the different types that may follow the proposed universal temperature profile in Fig. 6, we compare the fiducial temperature profile and observed deviations from this fiducial profile in Fig. 7. The top row shows the hybrid-bump type with no inner break (the temperature gradient is constant at $r < R_{\rm MAX}$). The second row shows the hybrid-bump type, but with an inner break (the temperature gradient is flatter at $r < R_{\rm BREAK}$), which indicates some internal heating as illustrated in the right-hand panel. The third row shows the double-break type where the temperature gradient is negative at $r < R_{\rm MIN}$, which indicates even stronger internal heating. The fourth row shows the hybrid-dip type where the profile ends before it reaches the peak. This type may be similar to the double-break type (the third row) and the lack of the peak may be caused by observational limitations and selection effects as described in the above.

Further extending the idea of the universal profile, we may explain the positive type (the bottom row in Fig. 7) as those of the hybrid-bump type (the top two rows in Fig. 7), but embedded in the hotter IGM/ICM such that the temperature peak of their own systems cannot be seen. This system might be similar to the hybrid-bump if the hot ISM could be separated from the hotter IGM/ICM. NGC 1400 (in the NGC 1407 group), NGC 4472, NGC 4406 (both in the Virgo cluster), and NGC 7626 (in the NGC 7619 group) are such an example. In particular, the temperature profile of NGC 4472 (the bottom panel of Fig. 7) shows that the profile starts off relatively flat before rising sharply at $r \sim 4$ kpc. At $r \sim 12$ kpc, the profile plateaus before rising sharply again due to the hot ICM. The inner break at ~4 kpc may be the same as the inner break in hybrid-bump type and the plateau at 12 kpc could be due to the ISM being washed out by the hotter ICM of the Virgo cluster. If the positive type is similar to the hybrid-bump type but embedded inside a hotter environment, the universal temperature profile can be applied to 49 out of 60 ETGs or 82 per cent of our sample.

The most obvious exception to the proposed universal temperature profile is the negative types, which do not fit the above explanations. Since this type is generally a small system with low $T_{\rm GAS}$ and $L_{\rm X,GAS}$ (see Fig. 5), one might consider this is an extreme case of a hybrid-dip type being truncated at $r < R_{\rm MIN}$ such that we could only see the inner negative gradient without the temperature minimum. NGC 1316 and NGC 4382 (see Appendix A) could be such an example as they show a hint of temperature rise at large radii, albeit with a large uncertainty. However, most galaxies in this type have the extended hot gas detected out to at least $r \sim 20$ kpc. The extent of the hot gas is considerably larger than $<R_{\rm MIN}> \sim$ 4 kpc, even larger than the largest $R_{\rm MIN}$ (~10 kpc in NGC 499). The most obvious examples are NGC 4125 and NGC 6482 where the temperature is constrained out to $r = 40$–50 kpc with no sign of a temperature gradient reversal. Also note that NGC 6482 has $L_{\rm X,GAS}$ and $T_{\rm GAS}$ that are comparable to that of the hybrid-bump type. The negative type may be similar to those of the non-cool-core (NCC) clusters, which are often found in disturbed systems, like mergers, and could have an irregular or declining temperature profile. However, NGC 6482 is one of the known relaxed, fossil systems (Khosroshahi et al. 2004), so it is quite different from the NCC clusters.

In summary, the temperature profiles of at least 72 per cent of our ETG sample (hybrid-bump, hybrid-dip, and double-break types) can be described by a universal temperature profile. In addition, if we consider that the positive types are embedded in a hotter IGM/ICM such that the temperature peak of the galaxy is not detected, then 82 per cent of our sample fits the universal temperature profile. The negative (13 per cent of our sample) and irregular (5 per cent) types do not fit the universal profile and require another explanation.

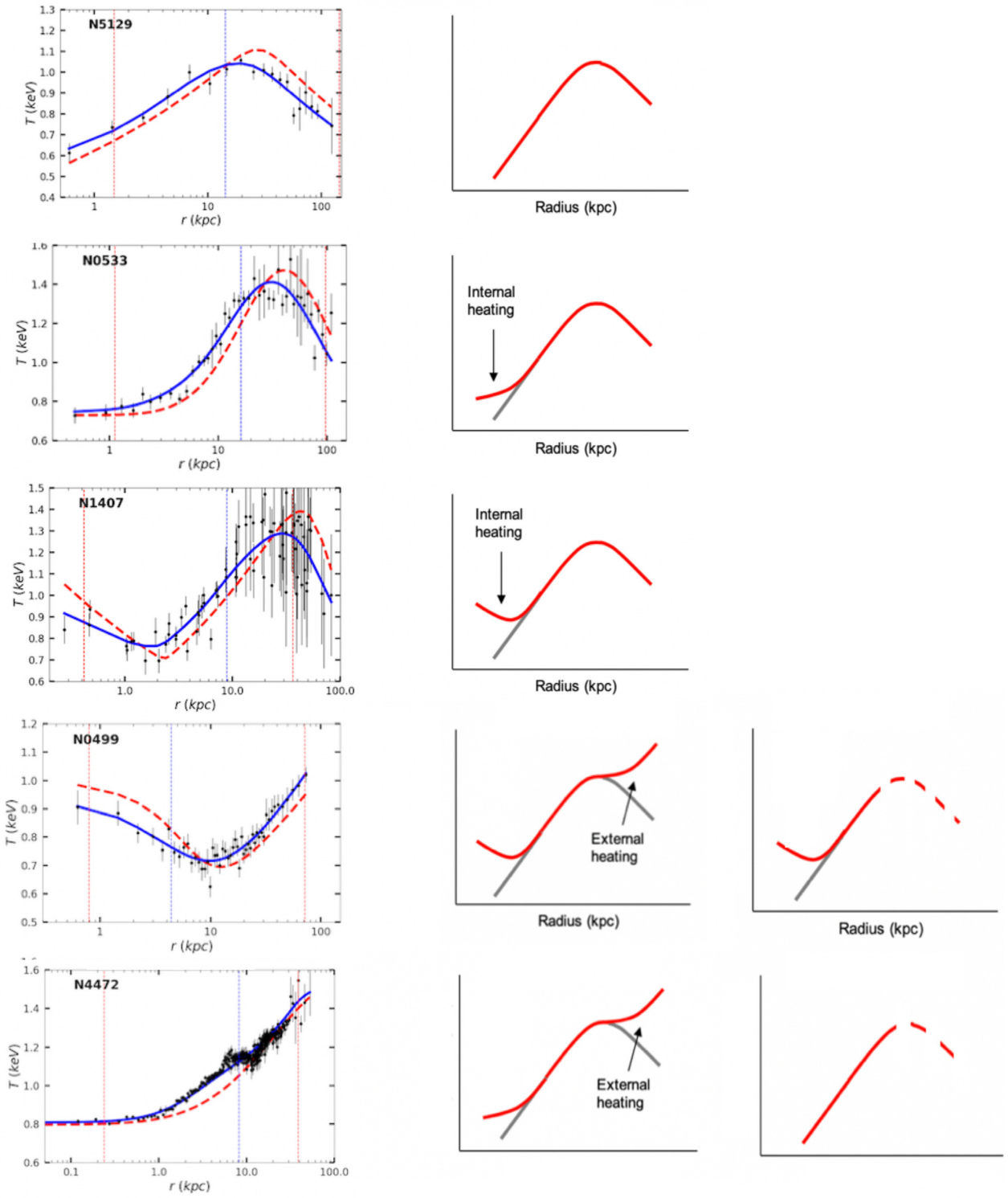

Figure 7. The left-hand panels show examples of hybrid-bump (without a break), hybrid-bump (with an inner break), double-break, hybrid-dip, and positive temperature profiles (top to bottom). The right-hand panels show a graphic illustration of how each profile may be explained by a 'universal' profile. The grey curve represents the fiducial profile and the red curve shows the observed profile with deviation from the fiducial profile.

6 DISCUSSION

Analysing the temperature profile of 60 ETGs, we have identified six profile types: in order of decreasing frequency of each type, hybrid-bump, hybrid-dip, negative, positive, double-break, and irregular. The hybrid-bump type is the majority (43 per cent) in our sample, but the hybrid-dip and negative types are likely underrepresented. Considering selection effects and observational limits, we find common characteristics of the temperature profile among 72 per cent (possibly up to 82 per cent), a temperature peaking at $R_{\rm MAX}$ and

declining inward and outward, except the inner temperature gradient inside $R_{\rm MIN}$ (or $R_{\rm BREAK}$), which can vary widely. We note that because ETGs and small groups are not easy to separate, our sample includes some small groups (but only those with $T_{\rm GAS} < 1.5$ keV).

X-ray studies of the hot gas in groups and clusters often separate them into two groups, cool cores (CCs) and non-cool cores (NCCs) (e.g. Molendi & Pizzolato 2001; Sanderson et al. 2009; Hudson et al. 2010). CCs are generally relaxed systems with cuspy cores and typically have higher metallicity and lower central temperature (T peaking at $\sim$0.1 $R_{\rm VIR}$ and declining towards the centre) and lower entropy than NCCs. NCCs are often disturbed systems, suggesting that they originate from mergers in denser environments or infalling substructures (McCarthy et al. 2011; Gaspari et al. 2014). Most ETGs in our sample belong to CC. As described in Section 3, those galaxies in the hybrid-bump, double-break, hybrid-dip, and positive have a positive temperature gradient (or a declining temperature profile towards the centre) in the region between $R_{\rm MIN}$ (or $R_{\rm BREAK}$) and $R_{\rm MAX}$ (or the observation limit). In this respect, 82 per cent of our sample belongs to CC, regardless of their inner temperature gradients (positive or negative). When the inner temperature gradient breaks, that occurs inside the CC, i.e. $R_{\rm MIN}$ is always smaller than $R_{\rm MAX}$ ($R_{\rm MIN} \sim 0.15 \times R_{\rm MAX}$).

The negative-type galaxies in our sample may be an analogue of the NCC clusters. NGC 1316 is a good example because it exhibits many signs of recent mergers (e.g. Schweizer 1980; Kim & Fabbiano 2003). However, the most obvious case with the temperature declining in a wide range of radii, NGC 6842, is known to be relaxed with no nearby possible perturber (a fossil system), in contrast to the disturbed NCC clusters.

T increases towards the centre for 42 per cent of our sample. We refer to these as *hot core* (HC) hereafter. Note that HC is not the opposite of CC. HC, if it exists, stays inside CC. Unlike the CC clusters where the hot gas properties are primarily controlled by the gravity, non-gravitational baryonic physics plays an important role in ETGs, most significantly in the inner region, possibly by additional heating (e.g. stellar feedback and AGN feedback). The stronger non-gravitational effect was previously demonstrated in the $L_{\rm X,GAS}$–$T_{\rm GAS}$ relation, which is considerably steeper in ETGs ($L \sim T^{4.5}$) than in clusters ($L \sim T^3$) (Kim & Fabbiano 2015). The same effect may be reflected in our finding that the peak of the temperature bump is found at a considerably smaller R ($\sim$0.04 $R_{\rm VIR}$) than that ($\sim$0.1 $R_{\rm VIR}$) in groups and clusters, and that the mean slope between the bumps and the inner break (or the dip) is $\sim$0.3, which is smaller than that (0.5) expected from the pure cooling flow (Gaspari et al. 2012) and that ($\sim$0.4) of CC clusters (e.g. Sanderson et al. 2006).

We note that the distribution of the inner T gradient is not bimodal, i.e. the slope varies continuously in our sample. The presence or absence of HC does not separate ETGs into two distinct groups, in contrast to the bimodality between CC and NCC clusters (e.g. Sanderson et al. 2009).

HC is often accompanied by a flattened surface-brightness profile at the core, which in turn causes a flatter density profile (less steeply increasing towards the centre, forming a core) and a flatter entropy profile (less steeply declining towards the centre, forming an entropy floor) than those without HC. Note that the density profile depends on accurate abundance measurements such that the density (and entropy) would look steeper (flatter) if a radial abundance gradient is ignored. We will present the full analysis of density and entropy profiles in the next paper.

6.1 The definition of $\nabla T_{\rm CORE}$

In Sections 4 and 5, we show that the inner temperature gradient varies widely from one galaxy to another. To further investigate the inner temperature profile inside $R_{\rm MIN}$ (or $R_{\rm BREAK}$), which is 3 (5) kpc on average, we measure the core temperature gradient ($\nabla T_{\rm CORE} = {\rm d}\log T/{\rm d}\log R$) at $r = 0.5$–1 kpc to explore the innermost hot gas property, but set a constraint on the minimum radius of 3′ to confidently remove any potential contamination by the nuclear emission. Out of 52 galaxies for which we measure $\nabla T_{\rm CORE}$, 25 galaxies have a negative $\nabla T_{\rm CORE}$ with HC (hybrid-dip, double-break, and negative types) and 27 galaxies have a positive $\nabla T_{\rm CORE}$ with no HC (hybrid-bump and positive types).

The presence of HC was previously known in a small number of ETGs (e.g. NGC 4278, Pellegrini et al. 2012b; NGC 4649, Humphrey et al. 2006 and Paggi et al. 2014; NGC 4552, Machacek et al. 2006), and in some groups (NGC 777 and NGC 5982, O'Sullivan et al. 2017). In this paper, we have systematically searched for HC and investigate them for the first time in a statistical manner. In particular, we explore the stellar feedback, AGN feedback, and gravitational heating for the cause of the HC in the following sections. DS08 have considered the outer temperature gradient associated with the environmental effect. We will address this question in the next paper with the additional *XMM–Newton* archival data.

6.2 $\nabla T_{\rm CORE}$–global hot gas properties

To investigate how the inner temperature gradient (or the presence or absence of HC) is related to other galaxy properties, we first plot $\nabla T_{\rm CORE}$ against $L_{\rm X,GAS}$ and $T_{\rm GAS}$ in Fig. 8. The different T-profile types are marked by different symbols and colours as in Fig. 5. As expected from Fig. 5, galaxies with a positive $\nabla T_{\rm CORE}$ (i.e. hybrid-bump and positive types) have higher $T_{\rm GAS}$ and $L_{\rm X,GAS}$ than those with a negative $\nabla T_{\rm CORE}$ (i.e. hybrid-dip and negative types). We applied the linear regression method[6] given by Kelly (2007). We also applied the Pearson and Spearman correlation tests taken from the SCIPY statistics package[7] to estimate the P-value for the null hypothesis. Based on the linear regression, we find a best-fitting slope of 0.68 ± 0.1 and 0.13 ± 0.02 for $T_{\rm GAS}$ and $L_{\rm GAS}$, respectively. Based on the two correlation tests, $\nabla T_{\rm CORE}$ is correlated with $T_{\rm GAS}$ and $L_{\rm X,GAS}$ at the 5σ–6σ level with the P-value ranging from 10^{-8} to 10^{-10}. The results are summarized in Table 4.

Given that the overall trends are driven by the fact that those with HC (negative gradient) are cooler and less luminous than those without HC, we further test the correlations for those with HC (HC subgroup) and without HC (nHC subgroup), separately. The correlation becomes less tight in both subsamples, but it is still significant (P-value = 0.06–0.0007) for the HC subgroup, while there is almost no correlation (P-value = 0.1–0.2) for the nHC subgroup. The correlation tests suggest that the presence of HC is more pronounced in smaller galaxies with lower $T_{\rm GAS}$ and $L_{\rm X,GAS}$. Regarding the inner break, its presence ($\nabla T_{\rm CORE} \sim 0$) or absence ($\nabla T_{\rm CORE} > 0$) among the hybrid-bump type has no preference in $T_{\rm GAS}$ and $L_{\rm X,GAS}$, once they are large enough.

We further explore the relation of $\nabla T_{\rm CORE}$ with other important galaxy parameters that may affect the core temperature gradient, including (Section 6.3) $L_{\rm K}$ indicating the stellar mass; the mean age indicating recent star formation; (Section 6.4) the radio luminosity

[6] https://github.com/jmeyers314/linmix
[7] http://www.scipy.org

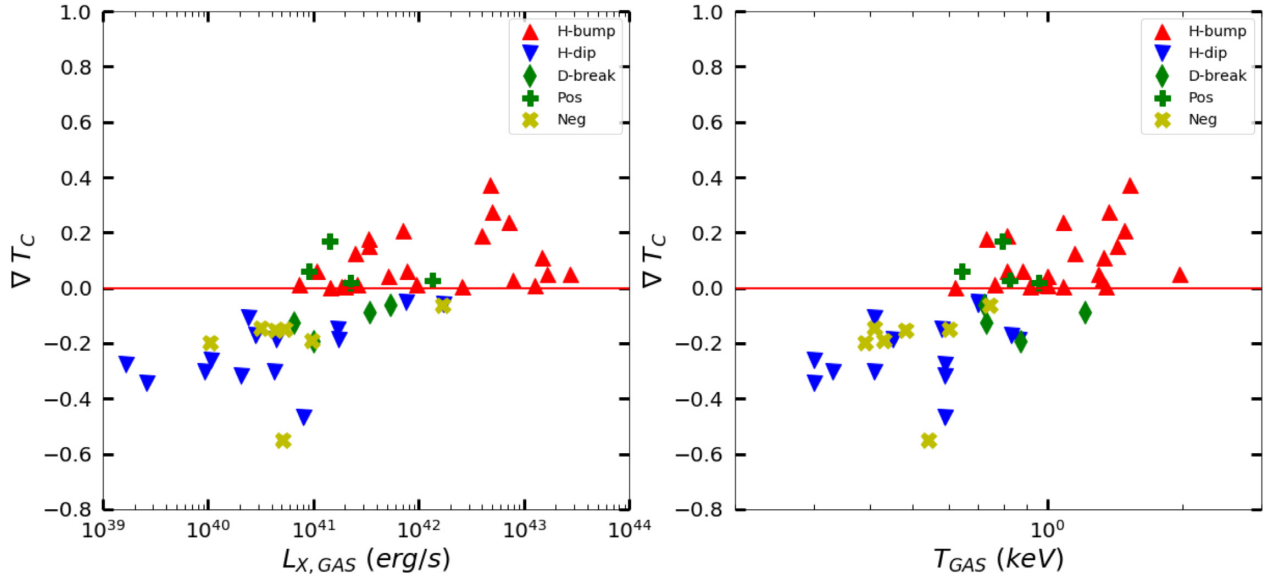

Figure 8. The inner T-gradient (∇T_{CORE}) against the temperature (T_{GAS}) and X-ray luminosity ($L_{X,GAS}$) of the hot gas. All the symbols are the same as in Fig. 5.

Table 4. Correlation test between ∇T_{CORE} and another variable.

	Number	linmix					Pearson		Spearman		
		Slope	Error	Intercept	Error	rms	P-value	σ	P-value	σ	
All types											
T_{GAS}	52	0.68	0.10	0.03	0.02	0.13	3.53e–09	**5.9**	3.07e–10	**6.3**	Fig. 8
L_{GAS}	52	0.13	0.02	– 5.36	0.85	0.14	2.60e–08	**5.6**	7.38e–10	**6.2**	Fig. 8
L_K	52	0.35	0.07	– 4.05	0.81	0.15	3.86e–06	**4.6**	2.42e–06	**4.7**	Fig. 9
Age	30	0.01	0.01	– 0.22	0.08	0.16	7.72e–02	1.8	5.54e–02	1.9	Fig. 9
$L_{1.4}$	45	0.06	0.02	– 1.66	0.47	0.16	9.66e–04	**3.3**	3.09e–04	**3.6**	Fig. 10
L_{AGN}	52	0.10	0.03	– 3.98	1.23	0.17	1.67e–03	**3.1**	3.77e–04	**3.6**	Fig. 10
M_{BH}	28	0.09	0.05	– 0.86	0.46	0.16	7.53e–02	1.8	2.75e–01	1.1	Fig. 10
V_{disp}	50	0.64	0.28	– 1.60	0.68	0.17	2.09e–02	**2.3**	1.32e–02	**2.5**	Fig. 11
M_{TOT}	29	0.32	0.09	– 3.90	1.06	0.15	5.59e–04	**3.5**	5.78e–04	**3.4**	Fig. 11
With a hot core (H-dip + Neg + D-break)											
T_{GAS}	25	0.31	0.17	– 0.12	0.05	0.12	6.03e–02	1.9	2.02e–02	**2.3**	Fig. 8
L_{GAS}	25	0.09	0.03	– 3.80	1.29	0.11	5.36e–03	**2.8**	6.87e–04	**3.4**	Fig. 8
L_K	25	0.18	0.08	– 2.25	0.85	0.11	1.34e–02	**2.5**	1.75e–02	**2.4**	Fig. 9
Age	19	0.01	0.01	– 0.25	0.07	0.12	2.78e–01	1.1	1.62e–01	1.4	Fig. 9
$L_{1.4}$	24	0.03	0.02	– 1.13	0.55	0.12	7.46e–02	1.8	5.36e–02	1.9	Fig. 10
L_{AGN}	25	0.03	0.04	– 1.27	1.44	0.13	4.26e–01	0.8	5.61e–01	0.6	Fig. 10
M_{BH}	16	0.04	0.05	– 0.58	0.42	0.12	3.06e–01	1.0	2.54e–01	1.1	Fig. 10
V_{disp}	25	0.28	0.30	– 0.87	0.71	0.13	3.18e–01	1.0	3.41e–01	1.0	Fig. 11
M_{TOT}	20	0.23	0.07	– 2.90	0.89	0.11	2.54e–03	**3.0**	2.09e–03	**3.1**	Fig. 11
No hot core (H-bump + Pos)											
T_{GAS}	27	0.24	0.16	0.09	0.02	0.10	1.18e–01	1.6	1.89e–01	1.3	Fig. 8
L_{GAS}	27	0.03	0.03	– 1.20	1.10	0.10	2.11e–01	1.3	2.35e–01	1.2	Fig. 8
L_K	27	0.11	0.10	– 1.15	1.13	0.10	2.32e–01	1.2	1.07e–01	1.6	Fig. 9
Age	11	0.00	0.01	0.04	0.09	0.07	6.05e–01	0.5	8.94e–01	0.1	Fig. 9
$L_{1.4}$	21	−0.02	0.02	0.59	0.48	0.08	2.48e–01	1.2	4.69e–01	0.7	Fig. 10
L_{AGN}	27	0.02	0.03	– 0.77	1.24	0.10	4.51e–01	0.8	2.86e–01	1.1	Fig. 10
M_{BH}	12	0.02	0.05	– 0.07	0.48	0.07	7.22e–01	0.4	9.39e–01	0.1	Fig. 10
V_{disp}	25	−0.34	0.24	0.91	0.59	0.08	1.39e–01	1.5	6.09e–01	0.5	Fig. 11
M_{TOT}	9	0.03	0.22	– 0.32	2.71	0.10	8.26e–01	0.2	3.81e–01	0.9	Fig. 11

Note. • All tests were done between ∇T_{CORE} and the logarithm values in the first column, as in Figs 8–11.
• σ is the Gaussian-equivalent significance, assuming that the P-value is the double-side probability at $|x| > \sigma$ of the normal distribution. σ is marked as a boldface when P-value < 0.05.

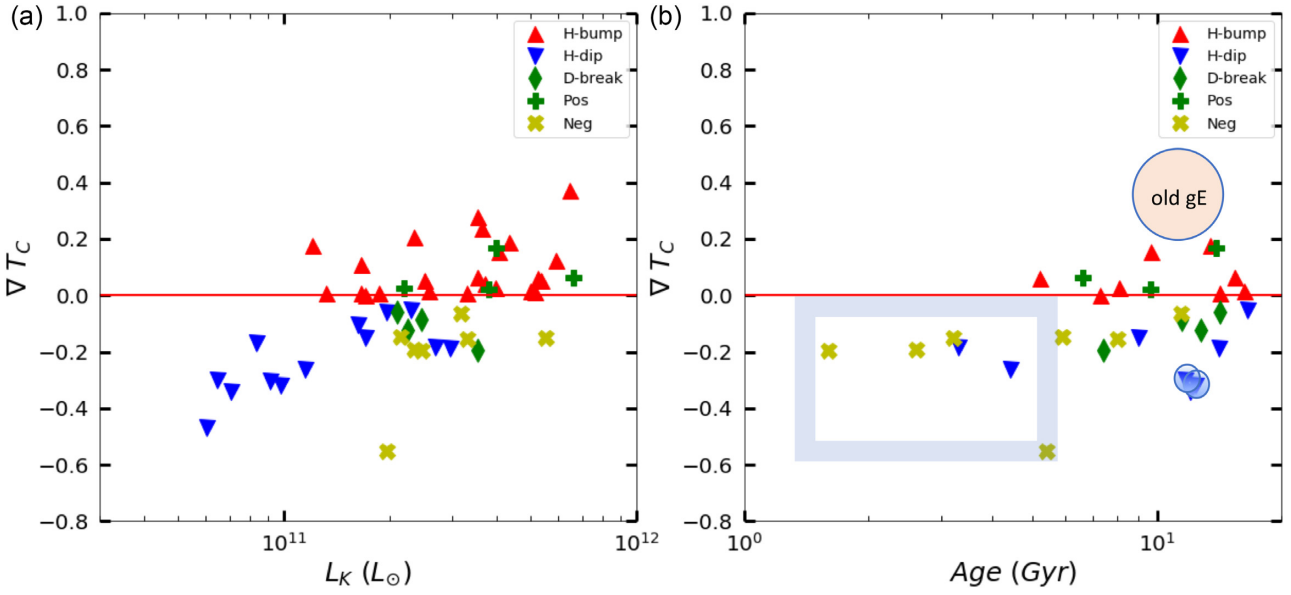

Figure 9. The core T-gradient ($\nabla T_{\rm CORE}$) against (a) the K-band luminosity and (b) the stellar age. All the symbols are the same as in Fig. 5.

at 1.4 GHz and the hard X-ray core luminosity both indicating the strength of the nuclear activity; (Section 6.5) the central stellar velocity dispersion indicating the dynamical mass in the core; and the total mass indicating the virial mass. All quantities and their sources are listed in Table 1.

6.3 $\nabla T_{\rm CORE}$–stellar properties

The left-hand panel of Fig. 9 shows the relation between the core temperature gradient and the stellar K-band luminosity ($L_{\rm K}$). $L_{\rm K}$ is a good proxy for stellar mass because the stellar mass-to-light ratio for ETGs ($M_{\rm STAR}/L_{\rm K}$ in unit of M/L) is close to 1 (e.g. Bell et al. 2003). $\nabla T_{\rm CORE}$ is closely correlated to the stellar K-band luminosity at the 5σ level. As in Fig. 8, the fact that the hybrid-bump and positive types are generally larger than the hybrid-dip and negative types drives the overall trend. For the HC subgroup, the correlation remains strong with the P-value of 0.01–0.02 or at the $\sim 2.5\sigma$ level, but for the nHC subgroup, the high P-value (0.1–0.2) indicates almost no correlation. This further suggests that the heating source in the core is most efficient in the smallest system.

In the right-hand panel of Fig. 9, we plot $\nabla T_{\rm CORE}$ against the stellar age. The correlation is weak, if any. The P-value is rather high (0.06–0.08). However, interestingly, all young galaxies with age <5 Gyr (inside the box in Fig. 9b) have a negative $\nabla T_{\rm CORE}$, i.e. they have HC, possibly suggesting that the recent star formation may cause the HC phenomenon. The single stellar population (SSP) equivalent age of a few Gyr may actually mean that a smaller fraction ($\sim$5 per cent) of the stellar mass is contained in an even younger population formed during the past $<\sim$1 Gyr (e.g. Serra & Oosterloo 2010), because the SSP age is strongly biased towards the age of the youngest stars (see Serra & Trager 2007). The stellar feedback from these rejuvenated young stars at the central region may provide an additional heating source.

It is still possible that recently formed stars may be embedded and hidden in some of the old galaxies. We further searched for the indirect evidence of recent star formation from the Atlas 3D (Cappellari et al. 2011) and Massive (Ma et al. 2014) surveys, both of which have extensively observed their sample ETGs in multiwavelength facilities. Among our sample, 13 and 17 galaxies are in the Atlas 3D and Massive surveys, respectively. Since molecular clouds are the birthplace of stars, we looked for the CO detections and found one galaxy each from two surveys, NGC 4477 with $M_{\rm H2} = 3 \times 10^7$ M$\odot$ (Young et al. 2011) and NGC 383 with 1.7×10^9 M$\odot$ (Davis et al. 2019). Similarly, one galaxy (NGC 4278) was detected in H I ($M_{\rm H\,I} = 10^6$ M$\odot$) in the core (Young et al. 2014). Note that we are considering the core H I detection, because the extended H I may not be directly related to the star formation. Interestingly, two galaxies (NGC 4278 and NGC 4477) have negative $\nabla T_{\rm CORE}$ and one (NGC 383) has $\nabla T_{\rm CORE} = 0.02$, only slightly above 0. In Fig. 9(b), the first two galaxies are marked by a large blue circle. NGC 383 does not have an age measurement. We also searched for the presence of dust, but none of the 13 galaxies in the Atlas sample have dust (Krajnovic et al. 2011).

We note that many galaxies with positive $\nabla T_{\rm CORE}$ do not have age measurements, because the X-ray luminous galaxies (mostly hybrid-bump type) are often at larger distances than the X-ray faint galaxies due to the selection effect. Considering the tendency of the giant E (gE) galaxies that they are old systems, we mark the likely location of these old X-ray luminous galaxies in Fig. 9, but this needs to be confirmed. O'Sullivan et al. (2017) also suggested that star formation is unlikely to be an enough heat source to significantly impact gas temperatures in dominant galaxies (BCGs) of groups.

In summary, $\nabla T_{\rm CORE}$ is strongly correlated with $L_{\rm K}$ (or $M_{\rm STAR}$), indicating that additional inner heating is most effective in small systems. There is a possible hint that stellar feedback from recent star formation could be related to the internal heating mechanism of HC.

6.4 $\nabla T_{\rm CORE}$–AGN

To explore the AGN feedback in terms of its effect on the core temperature gradient, we first use the 1.4 GHz radio luminosity. The radio data were primarily taken from the collection of Brown et al. (2011) and supplemented by the NVSS of Condon et al. (1998). Because $L_{1.4\,\rm GHz}$ is from the entire radio core and lobes, the radio emission of some galaxies with large radio lobes may not

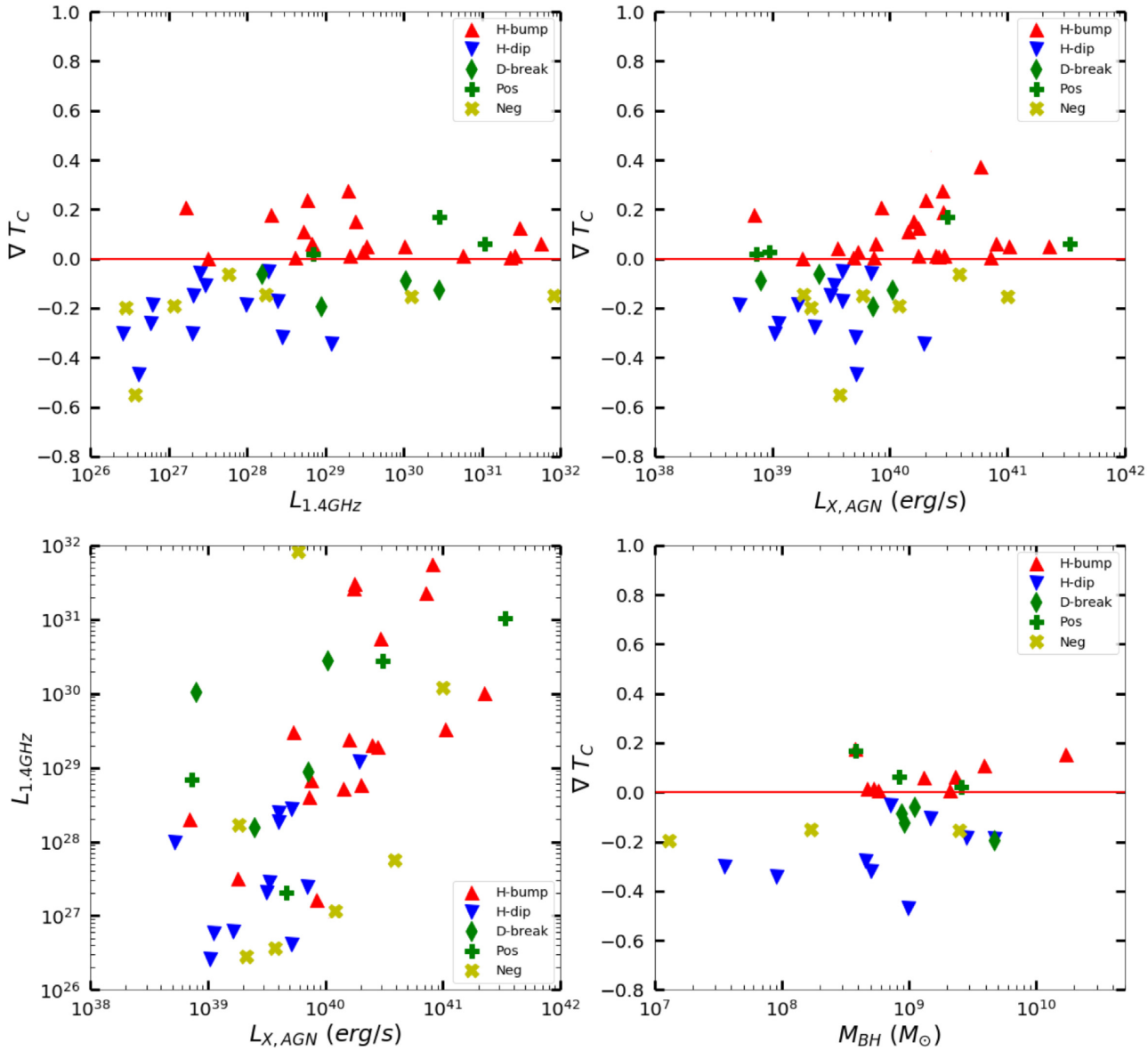

Figure 10. The core T-gradient ($\nabla T_{\rm CORE}$) against (top left) $L_{1.4\,\rm GHz}$, (top right) $L_{\rm X,AGN}$, and (bottom right) $M_{\rm BH}$. In the bottom-left panel, $L_{1.4\,\rm GHz}$ is compared with $L_{\rm X,AGN}$. All the symbols are the same as in Fig. 5.

directly indicate the current AGN status. For example, for NGC 1316 (Fornax A), which is most luminous in our sample (the yellow x with the extreme $L_{1.4} \sim 10^{32}$ erg s^{-1} Hz^{-1} in Fig. 10a), the core radio emission is only a small fraction of the total radio luminosity.

Another measure of the AGN strength is the X-ray luminosity at the galaxy centre. In the CGA program (Kim et al. 2019a), we applied two-component spectral fitting with an APEC model for the soft component from the hot gas and a power-law model for the hard component from the point sources including LMXBs and AGNs. We extract the hard component of the X-ray luminosity at the core. Because our sample galaxies do not host a strong AGN, i.e. they are mostly low-luminosity AGNs, we select the extraction radius at 3′. This radius corresponds to the 96 per cent (92 per cent) encircled energy circle at 1.5 keV (4.5 keV) for an on-axis source so that the fraction of $L_{\rm X,AGN}$ falling outside this radius is negligible. Since the X-ray luminosity from the LMXBs is also peaked at the galaxy centre, we need to correct for it. We estimate the expected contribution from LMXBs by scaling from $L_{\rm K}$ as in Kim & Fabbiano (2013). The central (3′) region contains about ∼5 per cent (on average) of the total stellar light. For most cases, the contribution from LMXBs is negligible, but $L_{\rm X,AGN}$ may be reduced by a factor of 2 when it is below 10^{39} erg s^{-1}. In spite of the caveats of $L_{1.4\,\rm GHz}$ and $L_{\rm X,AGN}$, the two quantities are correlated with P-value $\sim 5 \times 10^{-5}$ (see the bottom-left panel of Fig. 10).

In the top row of Fig. 10, we plot $\nabla T_{\rm CORE}$ as a function of $L_{1.4\,\rm GHz}$ (top left) and $L_{\rm X,AGN}$ (top right). Both relations are at the $\sim 3\sigma$ level for the entire sample, but almost no correlation for the subsamples with or without HC, except a weak (2σ) correlation between $\nabla T_{\rm CORE}$ and $L_{1.4\,\rm GHz}$ for the HC subsample. We also test with MBH (the mass of supermassive blackhole; see Table 1) in the bottom-right panel in Fig. 10. Given the limited availability of the $M_{\rm BH}$ data, we do not see a distinct correlation for the entire sample, nor the subsamples (see more in Section 6.5).

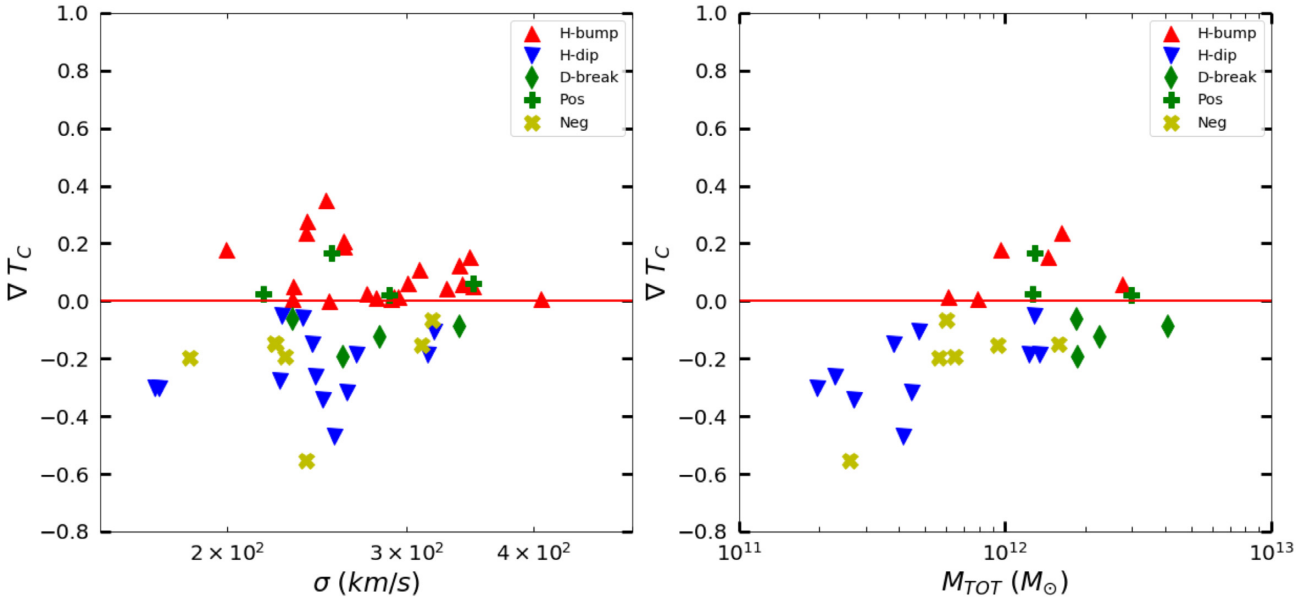

Figure 11. The inner T-gradient ($\nabla T_{\rm CORE}$) against the stellar velocity dispersion, $\sigma_{\rm v}$, and total mass, $M_{\rm TOT}$.

The interpretation of the correlation strength is somewhat ambiguous. However, one obvious finding is that if any correlation exists, it is in a positive sense for the entire sample and the HC subsample. Interestingly, this means that the weaker the AGN strength is (in $L_{1.4\,\rm GHz}$, $L_{\rm X,AGN}$, and $M_{\rm BH}$), the more pronounced the HC is. Therefore, we found no evidence that HC is caused by the effect of the current AGN feedback. This may not completely rule out the AGN effect. Under the conceivable AGN cycle, an AGN could have successfully heated its surroundings, shut off its own fuel supply, and become quiescent until cooling can build up a new reservoir of cold gas. However, even in this scenario, the hypothesis that the same galaxy evolves between HC and nHC is not supported, because the HC is preferentially found in small systems.

The weak negative correlation (P-value = 0.2–0.5) between $\nabla T_{\rm CORE}$ and $L_{1.4\,\rm GHz}$ for the nHC subsample (the red and green points in the top-left panel of Fig. 10) may be interpreted as a symptom of the AGN feedback, which plays a role in larger galaxies (e.g. in making the inner profile flatter for the hybrid-bump type), but the correlation is too weak and needs to be confirmed.

6.5 $\nabla T_{\rm CORE}$–$M_{\rm TOT}$

To explore a possibility that the HC may be produced by the gravitational heating as the hot gas cools and flows in, we further explore the relation with the central stellar velocity dispersion $\sigma_{\rm v}$ (as a measure of the inner dynamical mass) and the total mass ($M_{\rm TOT}$) of ETGs including stars and dark matter. We take $\sigma_{\rm v}$ primarily from the Atlas3D and Massive surveys and supplement from the literature (see the references in Table 1). For $M_{\rm TOT}$, we take the kinematically determined mass within 5 *Re* from Alabi et al. (2017) and supplement with those scaled from the mass of the globular cluster system ($M_{\rm GCS}$) assuming the near-linear relation between $M_{\rm TOT}$ and $M_{\rm GCS}$ (Kim et al. 2019b).

The correlation tests show $\sim$2.5σ ($\sim$3.5σ) correlations with $\sigma_{\rm v}$ ($M_{\rm TOT}$) for the entire sample (see Fig. 11). Again, this is primarily driven by the fact that the bigger (smaller) system has a positive (negative) $\nabla T_{\rm CORE}$. The correlations disappear in the subsamples, but the correlation between $\nabla T_{\rm CORE}$ and $M_{\rm TOT}$ remains strong ($\sim$3σ) for the HC subsample. This is in agreement with the correlations in Fig. 8 between $\nabla T_{\rm CORE}$ and the global hot gas properties ($L_{\rm X,GAS}$ and $T_{\rm GAS}$), which are known to be correlated with $M_{\rm TOT}$ (e.g. KF13 and Kim et al. 2019b). The meaningful correlations are all in a positive sense for the entire sample and the HC subsample. HC is more pronounced in galaxies with smaller $\sigma_{\rm v}$ and/or smaller $M_{\rm TOT}$. Our finding in this section, along with those in the previous section, i.e. only positive correlations with $M_{\rm STAR}$ (represented by $L_{\rm K}$) and $M_{\rm BH}$, indirectly suggests that the gravitational heating of inflowing gas is not the source of HC. This is also supported by O'Sullivan et al. (2017), who found that the inflow rates required for the central T rise in their group sample are unphysically high, a few solar masses per year.

Because the gravitational influence of the supermassive black hole may affect the hot gas temperature at the central region [see Humphrey et al. (2008) and (2009)], it is of interest to look for any correlation with $M_{\rm BH}$. However, $\nabla T_{\rm CORE}$ is not correlated with $M_{\rm BH}$, as seen in Fig. 10 (bottom right). It is still possible that we may not see this subtle effect because it works within $r <$ a few $\times$ 100 pc (e.g. Pellegrini et al. 2012a). As in Section 6.4, the only negative correlation between $\nabla T_{\rm CORE}$ and $\sigma_{\rm v}$ is for the nHC subsample, and it is very weak (P-value = 0.1–0.6). Again, this may be interpreted as a symptom of the gravitational heating in larger galaxies (e.g. in making the inner profile flatter for the hybrid-bump type), but this needs to be confirmed.

7 CONCLUSIONS

Examining the CGA (Chandra Galaxy Atlas) data products of 60 ETGs with extended hot haloes, we found the following results.

(i) We identify six different types of temperature profiles: 26 hybrid-bump (rising at small radii and falling at large radii), 13 hybrid-dip (falling at small radii and rising at large radii), 8 negative (falling all the way), 6 positive (rising all the way), 4 double-break (falling at small radii, rising at intermediate radii, and falling again at large radii), and 3 irregular types.

(ii) We find that the hot gaseous haloes of the majority of ETGs in our sample can be explained with a universal temperature profile. For the hybrid-bump, hybrid-dip, and double-break types, the mean galacto-centric distance of the T peak is at $R_{\rm MAX} = 35 \pm 25$ kpc (or $\sim$0.04 $R_{\rm VIR}$) and the mean distance of the T dip (or the inner break) is at $R_{\rm MIN}$ (or $R_{\rm BREAK}$) = 3–5 kpc (or $\sim$0.006 $R_{\rm VIR}$). The mean slope between $R_{\rm MIN}$ ($R_{\rm BREAK}$) and $R_{\rm MAX}$ is 0.3 ± 0.1.

(iii) The temperature gradient inside $R_{\rm MIN}$ (or $R_{\rm BREAK}$) varies widely, from negative, close to zero, to positive. The wide range of the core temperature gradient indicates the varying degree of additional heating at small radii. The HC inside $R_{\rm MIN}$ is most clearly visible for small galaxies. The nature of HC may be related to recent star formation, but we find no clear evidence that AGN feedback and gravitational heating play any significant role for HC.

(iv) The positive type may also fit the universal profile when observational limits and selection effects are taken into consideration.

(v) The negative and irregular types are exceptions and require another explanation.

ACKNOWLEDGEMENTS

We have extracted archival data from the *Chandra* Data Archive, and the data analysis was supported by the CXC CIAO software and CALDB. We have used the NASA NED and ADS facilities. The computations in this paper were conducted on the Smithsonian High Performance Cluster (SI/HPC). This work was supported by the Chandra GO grants (AR5–16007X), by Smithsonian Competitive Grant Program for Science, by Smithsonian 2018 Scholarly Study Program, and by NASA contract NAS8–03060 (CXC). LT acknowledges support from the Southampton-Smithsonian exchange program.

REFERENCES

Alabi A. B. et al., 2017, MNRAS, 468, 3949
Annibali F., Bressan A., Rampazzo R., Zeilinger W. W., Vega O., Panuzzo R., 2010, A&A, 519, 40
Babyk I. V., McNamara B. R., Nulsen P. E. J., Hogan M. T., Vantyghem A. N., Russell H. R., Pulido F. A., Edge A. C., 2018, ApJ, 857, 32
Bell E. F., McIntosh D. H., Katz N., Weinberg M. D., 2003, ApJS, 149, 289
Blakeslee J. P., Lucey J. R, Barris B. J., Hudson M. J., Tonry J. L., 2001, MNRAS, 327, 1004
Boehringer H., Voges W., Fabian A. C., Edge A. C., Neumann D. M. , 1993, MNRAS, 264, L25
Boroson B, Kim D.-W., Fabbiano G., 2011, ApJ, 729, 12
Brown M. J. I. et al., 2011, ApJ, 731, L41
Cappellari M. et al., 2011, MNRAS, 413, 813
Cappellari M. et al., 2013, MNRAS, 432, 1709
Churazov E., Brüggen M., Kaiser C. R., Böhringer H., Forman W., 2001, ApJ, 554, 261
Ciotti L. et al., 1991, ApJ, 376, 380
Ciotti L. et al., 2017, ApJ, 835, 15
Condon J. J. et al., 1998, AJ, 115, 1693
Davis T. A., Greene J. E., Ma C.-P., Blakeslee J. P., Dawson J. M., Pandya V., Veale M., Zabel N., 2019, MNRAS, 486, 1404
De Grandi S., Molendi S., 2002, ApJ, 567, 163
Denicolo G., Terlevich R., Terlevich E., Forbes D. A., Terlevich A., Carrasco L., 2005, MNRAS, 356, 1440
Dickey J. M., Lockman F. J., 1990, ARA&A, 28, 215
Diehl S., Statler T. S., 2006, MNRAS, 368, 497
Diehl S., Statler T. S., 2008, ApJ, 687, 986
Fabian A. C., 1994, ARA&A, 32, 277
Fabian A. C., 2012, ARA&A, 50, 455
Fasano G., Franceschini A., 1987, MNRAS, 225, 155
Gaspari M., Ruszkowski M., Sharma P., 2012, ApJ, 746, 94
Gaspari M., Churazov E., Nagai D., Lau E. T., Zhuravleva I., 2014, A&A, 569, A67
Gaspari M. et al., 2019, ApJ, 884, 169
Gastaldello F. et al., 2007, ApJ, 669, 158
Gastaldello F., Buote D. A., Brighenti F., Mathews W. G., 2008, ApJ, 673, L17
Goulding A. D. et al., 2016, ApJ, 826, 167
Grevesse N., Sauval A. J., 1998, Space Sci. Rev., 85, 161
Gültekin K. et al., 2009, ApJ, 698, 198
Helsdon S. F., Ponman T. J., 2003, MNRAS, 340, 485
Hudson D. S. et al., 2010, A&A, 513A, 37
Humphrey P. J. et al., 2006, ApJ, 646, 899
Humphrey P. J. et al., 2008, ApJ, 683, 161
Humphrey P. J. et al., 2009, ApJ, 703, 1257
Jensen J. B., Tonry J. L., Barris B. J., Thompson R. I., Liu M. C., Rieke M. J., Ajhar E. A., Blakeslee J. P., 2003, ApJ, 583, 712
Johansson P. H., Naab T., Ostriker J. P., 2009, ApJ, 697, L38
Kelly B. C., 2007, ApJ, 665, 1489
Khosroshahi H. G., Jones L. R., Ponman T. J., 2004, MNRAS, 349, 1240
Kim D.-W., Pellegrini S., 2012 'Hot ISM in Elliptical Galaxies' Astrophysics and Space Science Library, Vol. 378. Springer, Berlin
Kim D.-W., Fabbiano G., 2003, ApJ, 586, 826
Kim D.-W., Fabbiano G., 2013, ApJ, 776, 116
Kim D.-W., Fabbiano G., 2015, ApJ, 812, 127
Kim D.-W. et al., 2019a, ApJS, 241, 36
Kim D.-W., James N., Fabbiano G., Forbes D., Alabi A., 2019b, MNRAS, 488, 1072
Kormendy J., Ho L. C., 2013, ARAA, 51, 511
Kraft R. P., Jones C., Nulsen P. E. J., Hardcastle M. J., 2006, ApJ, 640, 762
Krajnovi'c D. et al., 2011, MNRAS, 414, 2923
Kuntschner H. et al., 2010, MNRAS, 408, 97
Lauer T. R. et al., 2007, ApJ, 664, 226
McCarthy I. G. et al., 2011, MNRAS, 412, 1965
Ma C.-P., Greene J. E., McConnell N., Janish R., Blakeslee J. P., Thomas J., Murphy J. D., 2014, ApJ, 795, 158
Machacek M. et al., 2006, ApJ, 644, 155
Markevitch M. et al., 2003, ApJ, 583, 70
Molendi S., Pizzolato F., 2001, ApJ, 560, 194
O'Sullivan E., Vrtilek J. M., Harris D. E., Ponman T. J., 2007, ApJ, 658, 299
O'Sullivan E., David L. P., Vrtilek J. M., 2014, MNRAS, 437, 730
O'Sullivan E. et al., 2017, MNRAS, 472, 1482
Paggi A. et al., 2014, ApJ, 787, 134
Pellegrini S., 2012, in Kim D.-W., Pellegrini S., eds, Hot Interstellar Matter in Elliptical Galaxies. Springer, New York, p. 21
Pellegrini S., Ciotti L., Ostriker J. P., 2012a, ApJ, 744, 21
Pellegrini S., Wang J., Fabbiano G., Kim D.-W., Brassington N. J., Gallagher J. S., Trinchieri G., Zezas A., 2012b, ApJ, 758, 94
Prugniel P., Simien F., 1996, A&A, 309, 749
Randall S. W. et al., 2011, ApJ, 726, 86
Randall S. W. et al., 2015, ApJ, 805, 24
Roediger E., Kraft R. P., Machacek M. E., Forman W. R., Nulsen P. E. J., Jones C., Murray S. S., 2012, ApJ, 754, 147
Saglia R. P. et al., 2016, ApJ, 818, 47
Sánchez-Blázquez P., Gorgas J., Cardiel N., González J. J., 2006, A&A, 457, 809
Sanders J. S., 2006, MNRAS, 371, 829
Sanderson A. J. R., Ponman T. J., O'Sullivan E., 2006, MNRAS, 372, 1496
Sanderson A. J. R., O'Sullivan E., Ponman T. J., 2009, MNRAS, 395, 764
Sarazin C. L., Bahcall J. N., 1977, ApJS, 34, 451
Sarazin C. L., White R. E., III, 1987, ApJ, 320, 32
Schweizer F., 1980, ApJ, 237, 303
Serra P., Oosterloo T. A., 2010, MNRAS, 401, L29
Serra P., Trager S. C., 2007, MNRAS, 374, 769
Sun M. et al., 2009, ApJ, 693, 1142
Tang S., Wang Q. D., 2005, ApJ, 628, 205
Terlevich A. I., Forbes D. A., 2002, MNRAS, 330, 547

Thomas D., Maraston C., Bender R., Mendes de Oliveira C., 2005, ApJ, 621, 673
Tonry J. L., Dressler A., Blakeslee J. P., Ajhar E. A., Fletcher A. B., Luppino G. A., Metzger M. R., Moore C. B., 2001, ApJ, 546, 681
Trager S. C., Faber S. M., Worthey G., González J. J., 2000, AJ, 120, 165
Tully R. B. et al., 2013, AJ, 146, 86
Vikhlinin A., 2006, ApJ, 640, 710
Vikhlinin A. et al., 2005, ApJ, 628, 655
Vikhlinin A. et al., 2006, ApJ, 640, 691
Young L. M. et al., 2011, MNRAS, 414, 940
Young L. M. et al., 2014, MNRAS, 444, 3408

APPENDIX A

The temperature profiles of individual galaxies are grouped by the profile type. The red line is the parametrized 3D temperature model, and the blue line is the best-fitting projected profile. The inner red vertical line indicates $r = 3'$, where the AGN could affect the temperature measurement, and the outer red line indicates the maximum radius where the hot gas emission is reliably detected with an azimuthal coverage larger than 95 per cent. The blue vertical line is at one effective radius.

1. Hybrid-bump

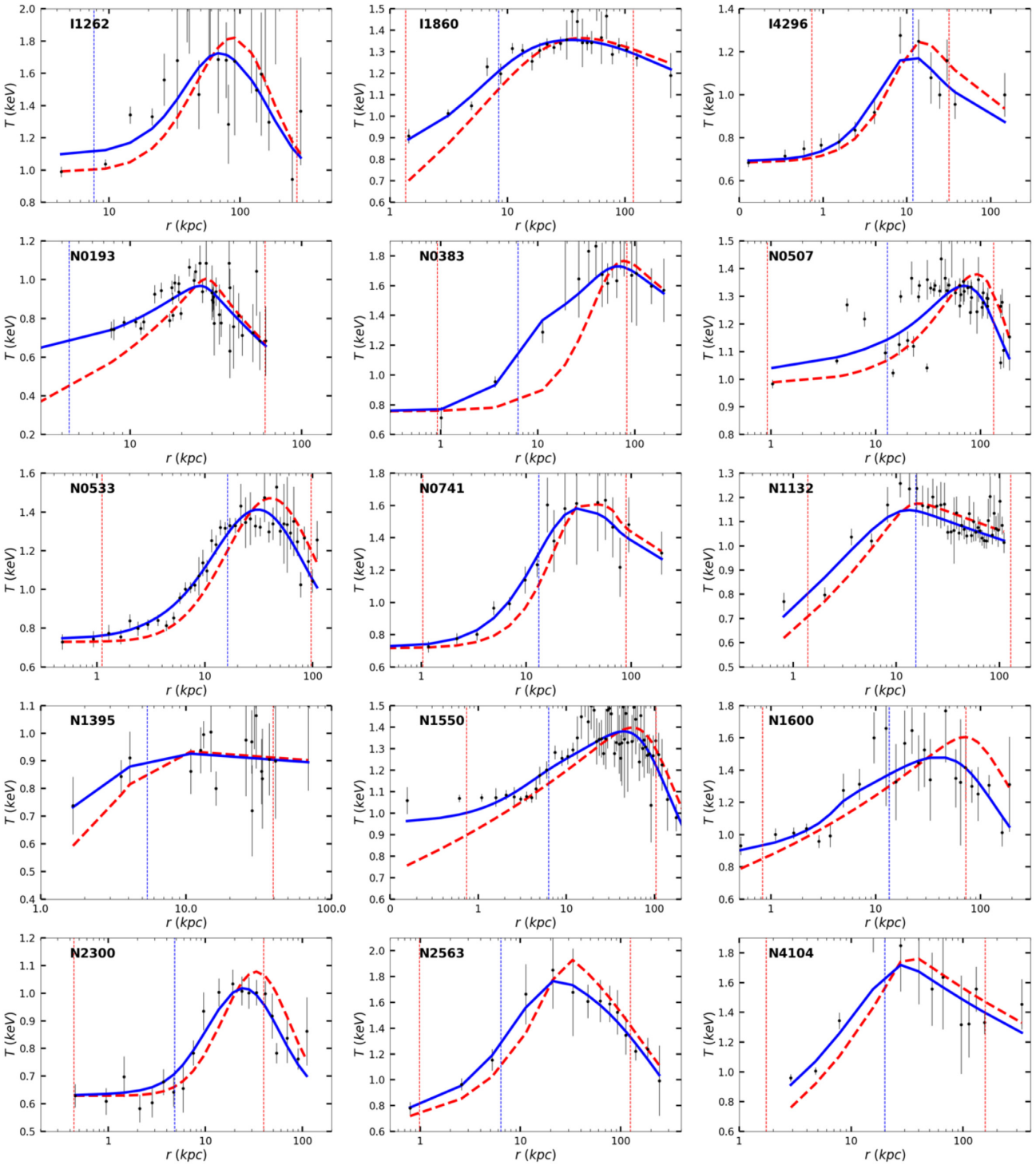

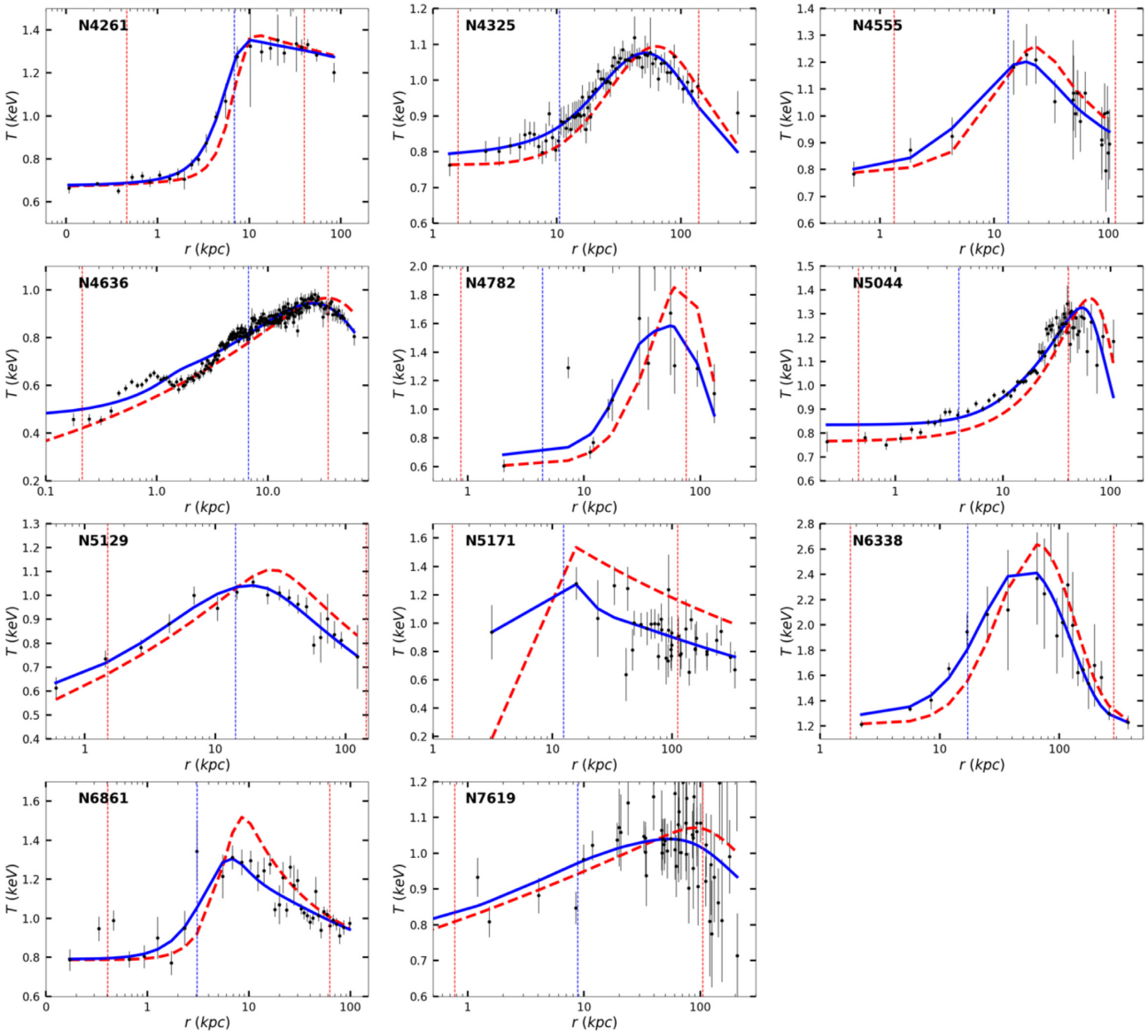

2. Hybrid-Dip

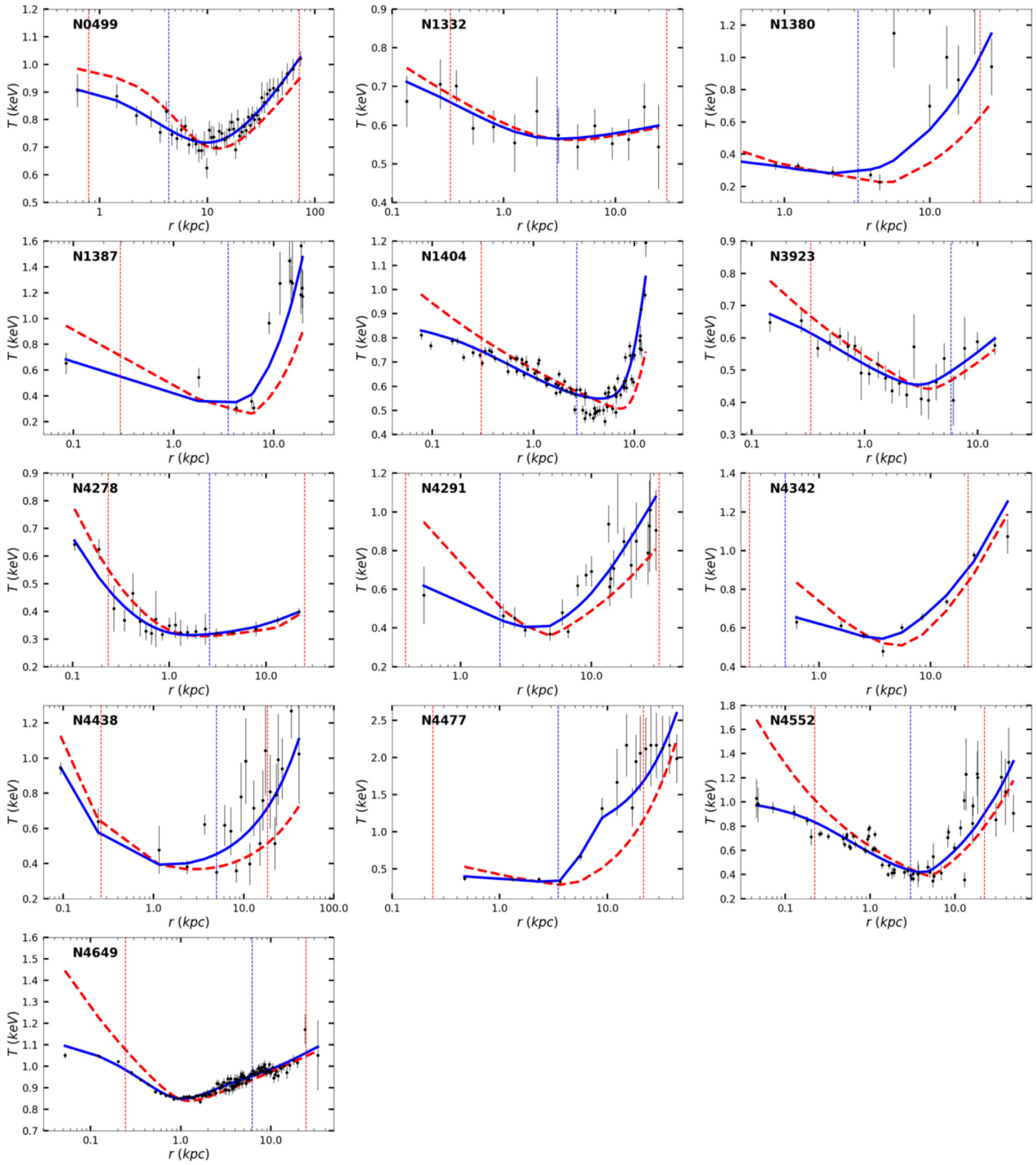

3. Double-Break

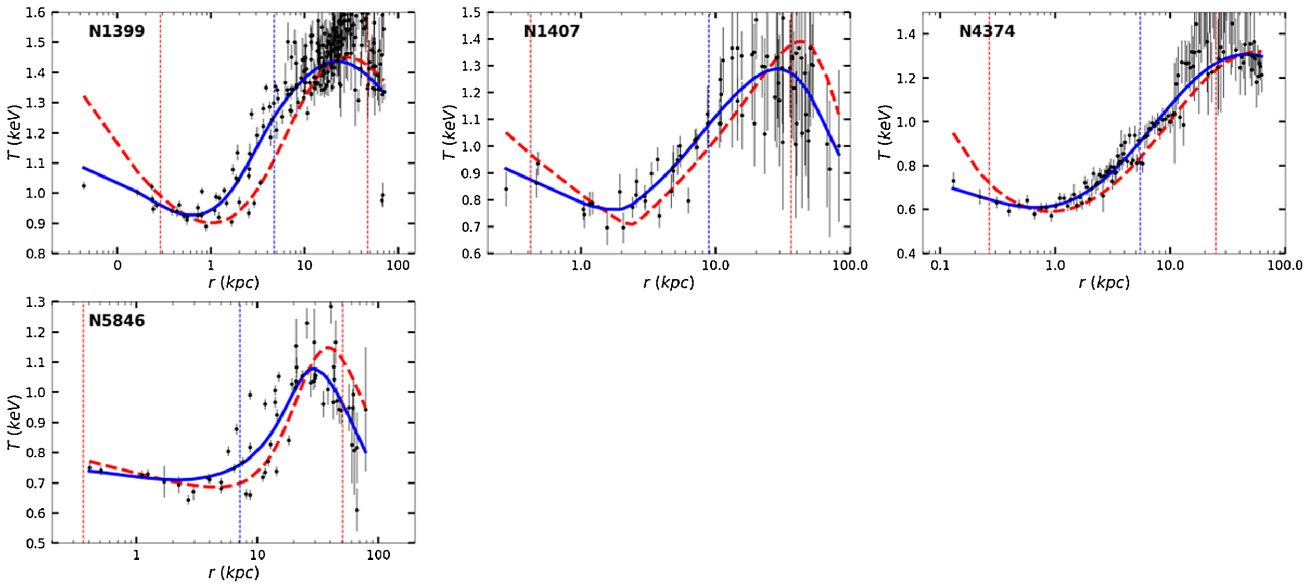

4. Positive

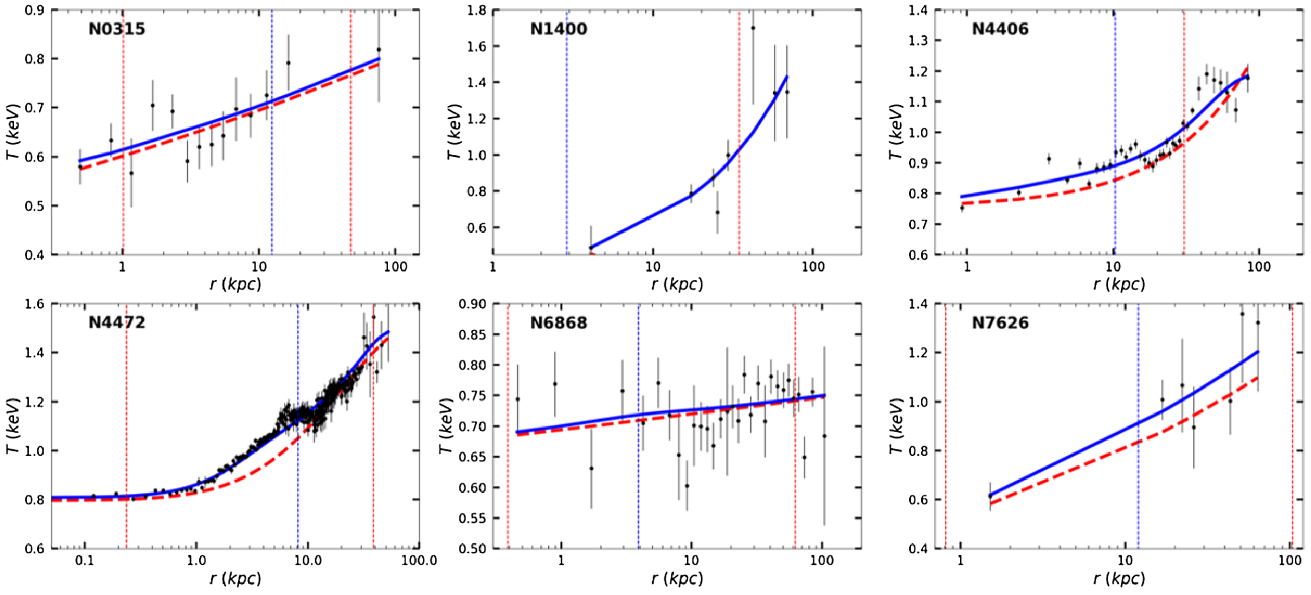

5. Negative

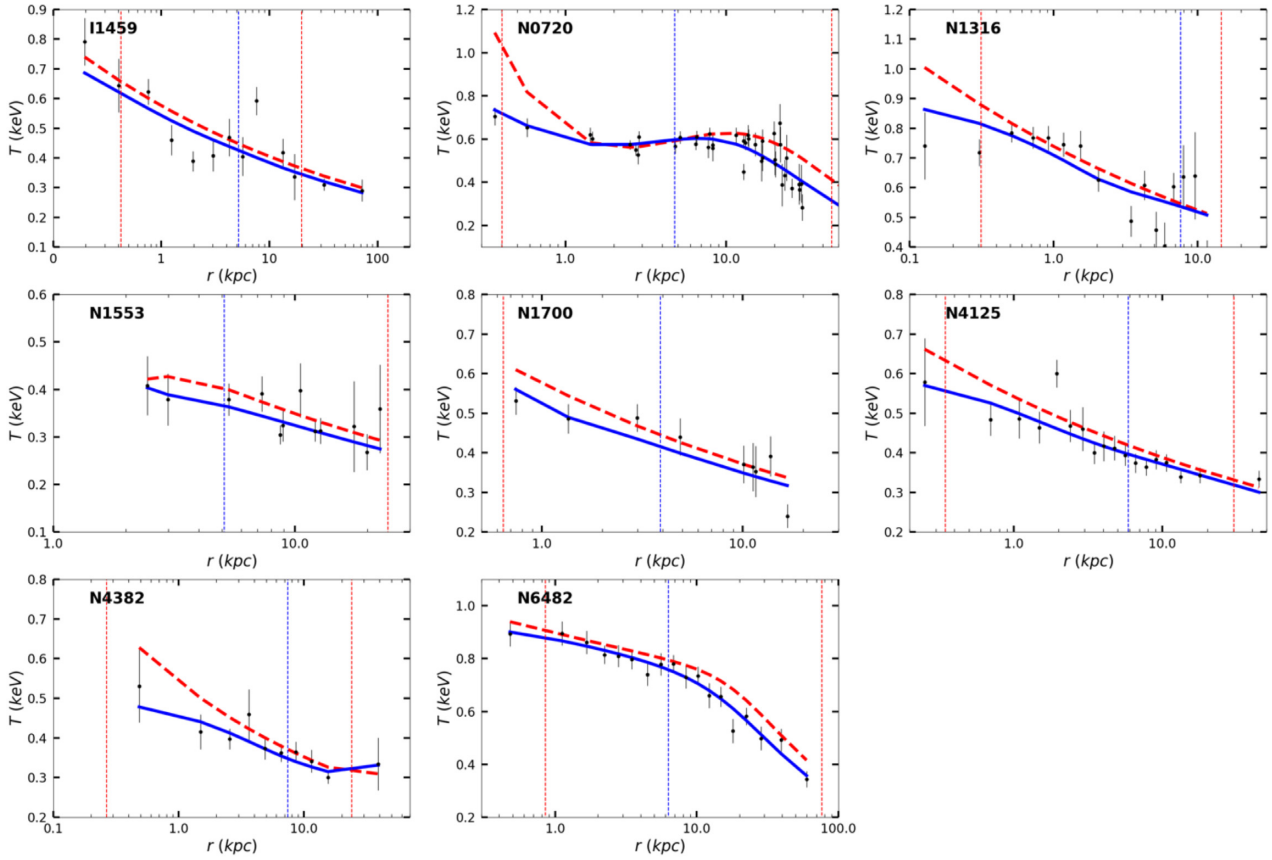

6. Irregular

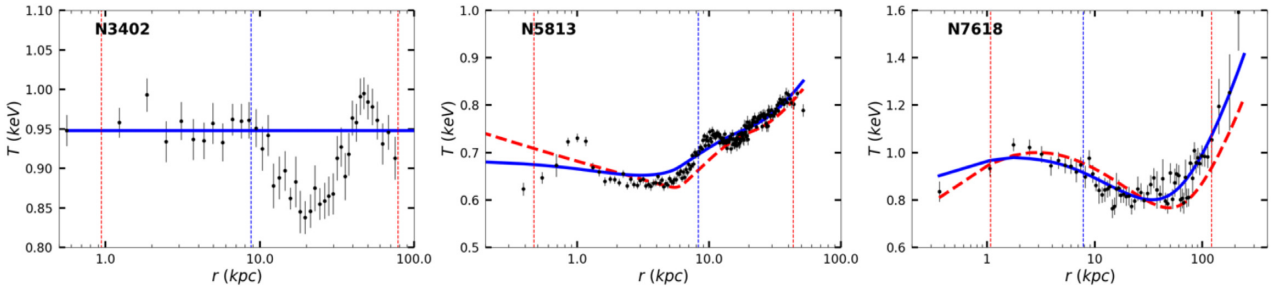

This paper has been typeset from a Microsoft Word file prepared by the author.